https://doi.org/10.5194/egusphere-2025-5601
Preprint. Discussion started: 5 March 2026

UAV-based Ultra High-Resolution Geodetic Mass Change Estimations near Schirmacher Oasis in East Antarctica: Insights from Sub-seasonal, Seasonal and Annual Timescales

Ajay Godara, P. Jayaraman Navinkumar, Tirthankar Ghosh, RAAJ Ramsankaran*

Hydro-Remote Sensing Applications (H-RSA) Group, Department of Civil Engineering, Indian Institute of Technology Bombay, Mumbai-400076

*Corresponding Author. RAAJ Ramsankaran; Email: ramsankaran@civil.iitb.ac.in

Abstract: This study presents an Uncrewed Aerial Vehicle (UAV) based framework to quantify surface elevation changes and subsequently geodetic mass change at high spatial and temporal resolution. The approach was demonstrated over a ~ 6.7 km^2 area near the Schirmacher Oasis, Dronning Maud Land, East Antarctica. High-resolution imagery derived from UAV allowed application of different pixel-wise snow and ice densities for precise geodetic mass change calculations. Sub-seasonal mass change values showed a gain of 0.539 cm w.e. during 17 November–3 December 2023 and a loss of –0.144 cm w.e. during 3–17 December 2023, highlighting the influence of short-term meteorological drivers such as temperature fluctuations, snowfall, and snow drift leading to snow redistribution over the ice surface. Over the seasonal period (17 November–17 December 2023), the geodetic mass change was found to be –0.141 cm w.e., while annual estimates exhibited a gain of +2.072 cm w.e. for the surveyed area, and +0.751 cm w.e. for a larger coverage (3 December 2023–21 November 2024. We validated the elevation change with in-situ stake measurements, which showed very good alignment. We also discuss key operational challenges such as flying in extreme weather conditions, battery limitations, and geolocation issues- and offer practical recommendations to improve the reliability and scalability of UAV-based monitoring in polar regions. With the suggested recommendations, the demonstrated framework can be applied to other polar sites to enhance understanding of ice sheet surface processes, to develop sites for calibration and validation of satellite-derived geodetic mass change products.

1 Introduction

The Antarctic Ice Sheet (AIS) is the largest freshwater reserve and currently the most extensive ice sheet on the planet. Antarctica's ice mass loss is one of the major contributors to sea level rise and also plays a crucial role in the Earth's climate system (Rignot et al., 2019). Glaciers and Ice Sheets (which include Antarctica and Greenland) across the globe are experiencing continuous mass loss due to enhanced global air temperatures and shifts in climatic patterns (Fretwell et al., 2012; Otosaka et al., 2023; Rignot et al., 2019; Rounce et al., 2023). The AIS holds enough volume of ice, which, upon melting, could translate into a sea level equivalent of approximately ~58m (Fretwell et al., 2012). Recently, a study by Edwards et al.,

https://doi.org/10.5194/egusphere-2025-5601
Preprint. Discussion started: 5 March 2026

(2021) estimated the rate of ice mass loss between 2003 and 2019 to be -118± 24 Gt y^{-1}, however, it is continuing to increase (IPCC, 2022).

Surface Mass Balance (SMB) refers to the net balance between the accumulation (primarily from solid precipitation) and ablation (due to surface melting and sublimation) on the surface of an ice sheet (Cuffey and Paterson, 2010). Studies suggest one of the major positive drivers of Antarctica's SMB is solid precipitation or snowfall (Lenaerts et al., 2016). However, a small perturbation in the surface mass balance plays a crucial role in regulating the meltwater's contribution to sea level rise. While much of Antarctica's ice loss occurs through subglacial melt and ice discharge at the ice-ocean boundary (DeConto and Pollard, 2016; Edwards et al., 2021; Sutter et al., 2016), SMB remains a critical factor in stabilising the ice sheet. Although satellite and model-based assessments have advanced our understanding of AIS's response to climate change, these are limited by coarse spatial resolution and a lack of in situ validation data. Traditional methods of measuring SMB- such as stake networks and snow pits- are often limited by logistical constraints, coarse spatial resolution and infrequent temporal coverage (Schlosser and Oerter, 2002). The remoteness, rugged topography, extreme weather conditions, and inaccessibility of these vast ice continents like AIS make it much more challenging. In this context, Uncrewed Aerial Vehicles (UAVs) which are commonly known as drones, that are remotely controlled and have recently emerged as a transformative tool in cryosphere research, offering high-resolution, repeatable, and cost-effective observations of surface elevation change and accumulation-ablation patterns (Immerzeel et al., 2014; Bhardwaj et al., 2016; Garg et al., 2023). It acts as an intermediate platform between satellite sensors and ground-based measurements/observations, providing centimetre-level spatial resolution data.

UAVs have emerged as versatile platforms for Antarctic research, with applications spanning terrestrial ecology, wildlife monitoring, atmospheric observations, and cryospheric science. Within glaciology, UAVs have proven particularly valuable for resolving fine-scale surface and near-surface processes that are difficult to capture using satellite sensors alone. Their centimetre-scale spatial resolution enables detailed mapping of glacier topography, crevasse fields, blue ice areas, and rapidly evolving surface features, often revealing patterns that remain unresolved or underestimated in spaceborne products (e.g., Bliakharskii et al., 2019; Markov et al., 2019). Beyond surface mapping, UAV-mounted geophysical sensors, such as dual-frequency radar systems, have also been deployed to investigate ice thickness and subglacial morphology, providing insights into ice dynamics in fast-flowing regions (Leuschen et al., 2014). UAV-derived digital elevation models (DEMs) have further been used to quantify surface subsidence and deformation associated with both surface and subsurface processes, highlighting their potential for monitoring short-term glacier dynamics (Florinsky and Bliakharskii, 2019). A comprehensive overview of these diverse applications was provided by (Pina and Vieira, 2022).

In the context of mass balance/mass change, UAV-based geodetic approaches remain comparatively rare but demonstrate considerable promise. Existing studies have shown that UAV-derived elevation changes can capture pronounced spatial heterogeneity in accumulation and ablation over short temporal scales (e.g., Bello et al., 2023). However, most of these investigations have been spatially limited, often restricted to small areas, and typically focus on single time windows. Moreover, UAV-based mass balance estimates commonly assume homogeneous surface densities, thereby neglecting the strong spatial and temporal variability between snow and ice surfaces that can substantially influence mass balance

https://doi.org/10.5194/egusphere-2025-5601
Preprint. Discussion started: 5 March 2026

calculations. Importantly, no previous studies have systematically examined geodetic mass balance variability across multiple temporal scales- from sub-seasonal to seasonal and annual using UAV datasets.

In this study, we address these gaps by demonstrating the use of UAV photogrammetry to estimate sub-seasonal, seasonal ("operational" Austral Summer 2023) and annual (November 2023– December 2024) geodetic mass change over a section of the Antarctic Ice Sheet near Schirmacher Oasis, Dronning Maud Land. UAV-derived geodetic mass change estimates are compared with in-situ stake measurements to show their accuracy. All the UAV surveys were conducted during the 43rd and 44th Indian Scientific Expedition to Antarctica (ISEA). We also discuss key operational challenges such as flying in extreme weather conditions, battery limitations, and geolocation issues- and offer practical recommendations to improve the reliability and scalability of UAV-based monitoring in polar regions.

2 Study Area and Fieldwork

2.1 Study Area

The study area is located at the ice-sheet frontal margin adjacent to Maitri Station, India's permanent Antarctic research station, located within the Schirmacher Oasis in central Dronning Maud Land (cDML), East Antarctica (Fig. 1). The region is subjected to harsh Antarctic climatic conditions. Summer temperatures may reach up to +5 °C, whereas winter temperatures routinely fall to –45 °C, with occasional extremes down to –60 °C. The local climate is dominated by strong katabatic winds, flowing from the Antarctic interior regions. The ~6.75 sq km, UAV-surveyed site (Fig. 1) lies close to the grounding line, where the Antarctic Ice Sheet transitions to the Nivlisen Ice Shelf. Additionally, the region is characterised by high snowfall which ranges from 200-600 mm/year (Lenaerts et al., 2013; Welker et al., 2014; Yu et al., 2025), substantial wind-driven snow accumulation (Birnbaum et al., 2010), and enhanced surface ablation processes, including sublimation and melting, particularly around the Schirmacher Oasis, the adjacent ice sheet margin, and the nearby ice shelf areas of cDML (Winther et al., 1996). The area is also marked by an extensive blue ice area (Sinharay, 2022). A runway is also located near to the study area, operated to support the transportation and logistics for nearby research stations. Collectively, these processes exert a strong influence on local surface mass balance, and the presence of a runway which requires regular maintenance, making it an important site for surface dynamic studies.

https://doi.org/10.5194/egusphere-2025-5601
Preprint. Discussion started: 5 March 2026

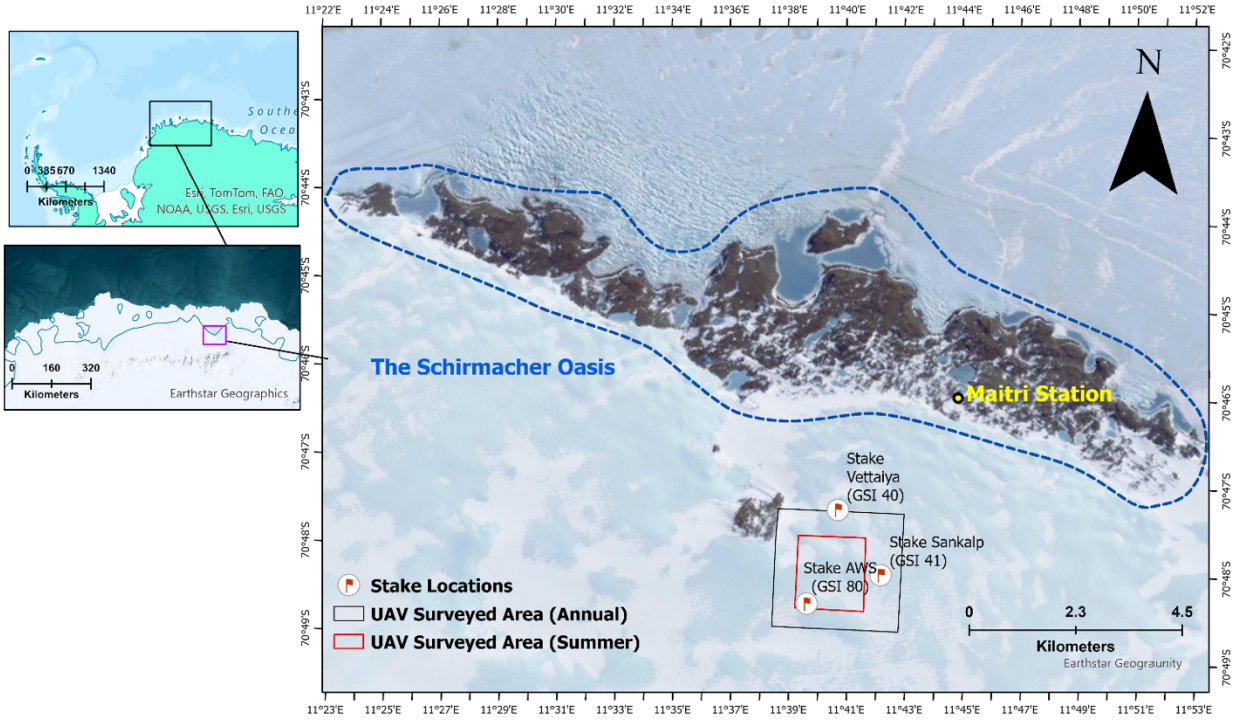

Figure 1: Study area map with the surveyed area marked in red (small areas) and black (larger area) boxes. The stake locations used for validation are also marked with their index as GSI 40, 41, and 80 (green and black markers). Indian Research Station-Maitri is located with the yellow marker and Schirmacher Oasis with blue dotted line (Basemap sources: Esri, Maxar, Earthstar Geographics, NOAA, USGS | Powered by Esri).

2.2 UAV Surveys and Data Collection

During the austral summer seasons of 2023 and 2024, as part of the 43rd and 44th Indian Scientific Expeditions to Antarctica (ISEA), four UAV surveys were conducted over a portion of the polar ice sheet near Schirmacher Oasis, Queen Maud Land, East Antarctica. Three UAV surveys were performed in November–December 2023, while a fourth survey was conducted in November 2024. The commercial off-the-shelf SenseFly eBee X fixed-wing UAV was used in this study, which is equipped with a 24 MP RGB SODA (Sensor Optimised for Drone Applications) payload. The SenseFly eBee X is a belly-landing UAV with RTK modules and obstacle sensors for landing. Here in this study, we have used the Emlid Reach RS2+ GNSS receiver to establish a temporary base station near to the UAV take-off location and ground control system. As the Emlid base station was installed on the ice surface during each survey and could not be operated continuously for long-duration positioning (e.g., 24-hour PPP) due to low temperatures and battery drainage, its initial coordinates required post-processing refinement. A Trimble R12 GNSS receiver was therefore installed near Maitri Station to be used as a reference base station. The Trimble R12 observations were used to correct the Emlid base station coordinates during post-processing. The corrected Emlid base station solution was then used to generate Post Processing Kinematics (PPK) correction for UAV, enabling accurate geotagging of high-resolution imagery.

https://doi.org/10.5194/egusphere-2025-5601
Preprint. Discussion started: 5 March 2026

An initial test flight was carried out on 16 November 2023, providing insights into battery drainage, gust effects, and landing performance in Antarctica's cold environment, resulting in coverage of a smaller area due to lower altitude. Considering UAV capabilities, three-four flights were strategically planned on each date, optimizing the flight take-off location from the centre. Based on this experience, subsequent flights utilized a fixed flying height of 260 meters, achieving a Ground Sampling Distance (GSD) of 6 cm.

The UAV flights were conducted through automated missions, which were planned using the E-motion application (https://eaglenxt.com/drone-software/emotion/). Due to the absence of high-resolution, accurate DEM data, the terrain-following mode was not employed, and all flights were executed at a fixed altitude relative to the take-off point. Given the dynamic nature of the snow and ice surfaces, each survey was completed within a single day to ensure temporal consistency. The amount of overlap was chosen based on initial trial experience and flight time optimisation. During November-December 2023, we could only manage to get 3 flights as detailed in Table 1. Following this period, the UAV got crashed and remained out of operation for several days. Subsequently, persistent strong winds in January hindered further flight operations. Based on our experience, we discussed this challenge and provided recommendations under section 5.4.

Based on the collected dataset, we categorized the observations into four temporal periods: two sub-seasonal windows (17 November–3 December 2023 and 3–17 December 2023), one seasonal window corresponding to the UAV operational timeframe (17 November–17 December 2023; austral summer), and one annual window (3 December 2023–21 November 2024). For the annual analysis, two spatial extents were considered: (i) a smaller region matching the UAV-survey footprint used in the sub-seasonal and seasonal analyses (Fig. 1, red outline), and (ii) a larger surrounding region (Fig. 1, black outline).

Table 1: Summary of UAV Survey acquisition parameters and flight details, such as number of images captured, flying height of the UAV, image overlap percentage (%), and number of images in PPK correction, and standalone processing for all the different survey dates.

Date	Flight No.	Images captured	Flying Height (meters)	Overlap (%)	PPK Corrected	Standalone
17 November 2023	1	1056	175	85	1044	12
	2	834	175	85	834	0
	3	658	175	85	658	0
	4	1154	175	85	1154	0
3 December 2023	1	807	260	85	807	0
	2	747	260	85	747	0
	3	822	260	85	822	0
17 December 2023	1	821	260	85	821	0
	2	755	260	85	755	0
	3	788	260	85	788	0
21 November 2024	1	681	260	85	681	0
	2	644	260	85	644	0
	3	752	260	85	752	0
	4	708	260	85	708	0

https://doi.org/10.5194/egusphere-2025-5601
Preprint. Discussion started: 5 March 2026

2.3 Mass Change Validation data

To validate the UAV-derived geodetic mass balance estimates, traditional in-situ stake measurements were used as direct measurements of surface accumulation and ablation over the corresponding survey period which would provide better insights into the reliability and accuracy of the UAV data. The stake network around Schirmacher Oasis was established and are maintained by the Geological Survey of India (GSI). Bamboo sticks were used as stakes and measurements were conducted on the same days as UAV surveys were carried out. The GCP locations of these stakes were used to co-register with the UAV-derived DEM grid, and elevation changes at each location were used for comparative analysis. Exposed height of stakes was measured on 17 Nov 2023, 3 Dec 2023, 17 Dec 2023 and then 21 Nov 2024. The corresponding elevation changes were then calculated for sub-seasonal 1, sub-seasonal 2, seasonal, and annual time scales. It shall be noted that the snow thickness at the stake location was negligible (less than 1 cm) during the measurement intervals, as the surface remained consistently snow-free (bare ice). Accordingly, using the measured elevation change, geodetic mass change was estimated for the three time periods by assuming an ice density (ρ_{ice} = 917 kg m^{-3}), because the stake location remained snow-free (blue ice) throughout the measurement intervals. It shall be noted that a constant ice density value was assumed here due to the lack of field-collected density data.

2.4 Meteorological data

The daily meteorological data in this study were obtained from an Automatic Weather Station (AWS) installed at the Indian Scientific Research Station- Maitri, operated and maintained by the India Meteorological Department (IMD). The AWS collects all the required data like temperature, wind speed, wind direction, wind chill, pressure, and relative humidity (RH). We also used daily precipitation measurements recorded using a measurement gauge set up by IMD. All the datasets are collected on an hourly basis. In this study, we used the Temperature, Precipitation, wind speed and wind direction for further analysis.

3 Methods

The methodological framework adopted in this study involved a systematic workflow for photogrammetric processing steps employed to derive high-resolution orthoimages and DEMs, and thereafter elevation change and geodetic mass change calculations. The details are given as follows.

3.1 DEM and Orthoimage Generation

The images collected from each UAV survey were processed using the Structure-from-Motion and Multi Stereo View (SfM-MVS) approach in Agisoft Metashape Professional 2.1.1 (Agisoft Metashape 2025). The proprietary software was used on a high-computation workstation with one Intel Xeon Gold 6348 CPU processor with 56 cores and 256 GB of random-access

https://doi.org/10.5194/egusphere-2025-5601
Preprint. Discussion started: 5 March 2026

memory. The standard workflow procedure in the Agisoft application was followed for orthoimage and DEM generation (Gindraux et al., 2017) with a few customizations at the tie point and point cloud filtering.

All flights from each survey date were combined and processed together to achieve a uniform point cloud. The UAV-acquired overlapping images with their geotags and platform data (roll, pitch, and yaw) were imported into the SfM-MVS workflow along with ground control points (GCPs) and check points (CPs). All imported overlapping images are aligned based on the geotag information of each image at highest accuracy settings. The alignment procedure involves feature detection, image matching, aerial triangulation, and bundle adjustment. This process estimates both external parameters (camera position and orientation) and internal parameters, generating a tie-point cloud as the triangulated output of matched feature points. The accuracy of the tie-point model directly influences the final DEM accuracy, since it depends on factors such as image overlap, image depth, and the geometric complexity of surface features. To control the erroneous surface matching caused by low contrast over snow and ice surface, we aligned the images at highest accuracy to generate dense key points and tie point model, additionally applied strict tie point and reprojection error filtering to eliminate poorly matched tie points. To ensure horizontal and vertical accuracy, we used GCPs to reference the SfM model and CPs for independent accuracy assessment. The GCP targets were surveyed in the field using a survey-grade GNSS receiver with PPK-corrected coordinates and were manually identified in multiple overlapping images. These GCP observations were then incorporated during camera self-calibration and bundle adjustment to optimize camera parameters and image alignment. In contrast, CPs were excluded from all optimization steps and reserved solely for validation. Multi-view stereo algorithm subsequently builds a dense point cloud from a sparse tie point cloud. The density of the final point cloud depends on the number and quality of matching key points. The depth maps were built upon point clouds, which were mildly filtered considering the surface characteristics in the study area. Finally, Digital Surface Models (DSM) and orthoimages with a grid size of 50cm were generated for sub-seasonal seasonal and annual elevation change analysis. Here the DSMs are considered as DEMs because the site represent bare earth features only. To evaluate the horizontal accuracy of DEMs and orthoimages, we compared the known horizontal coordinates of the CPs measured from the field using a survey grade GNSS receiver with positions extracted from the point cloud. Similarly, the vertical accuracy was quantified as the elevation difference between the point cloud models and the CPs. The achieved accuracy at checkpoints is given in Table 2.

Finally, to determine the accurate elevation difference between two DEMs, co-registration is necessary to eliminate systematic biases and ensure accurate alignment. The co-registration was accomplished through the stake's geolocations in the field.

3.2 Orthoimage Classification and Density Estimation

Here in this study, the distributed density estimation was carried out using a novel approach (Eq. 1). Previous studies have used either a constant density value for the study area or snow density for accumulation and ice density for ablation (Bello et al., 2023). However, the availability of high-resolution optical (shown in Fig. 2) and elevation change data from the same time enabled us to estimate the class-wise transition over time.

https://doi.org/10.5194/egusphere-2025-5601
Preprint. Discussion started: 5 March 2026

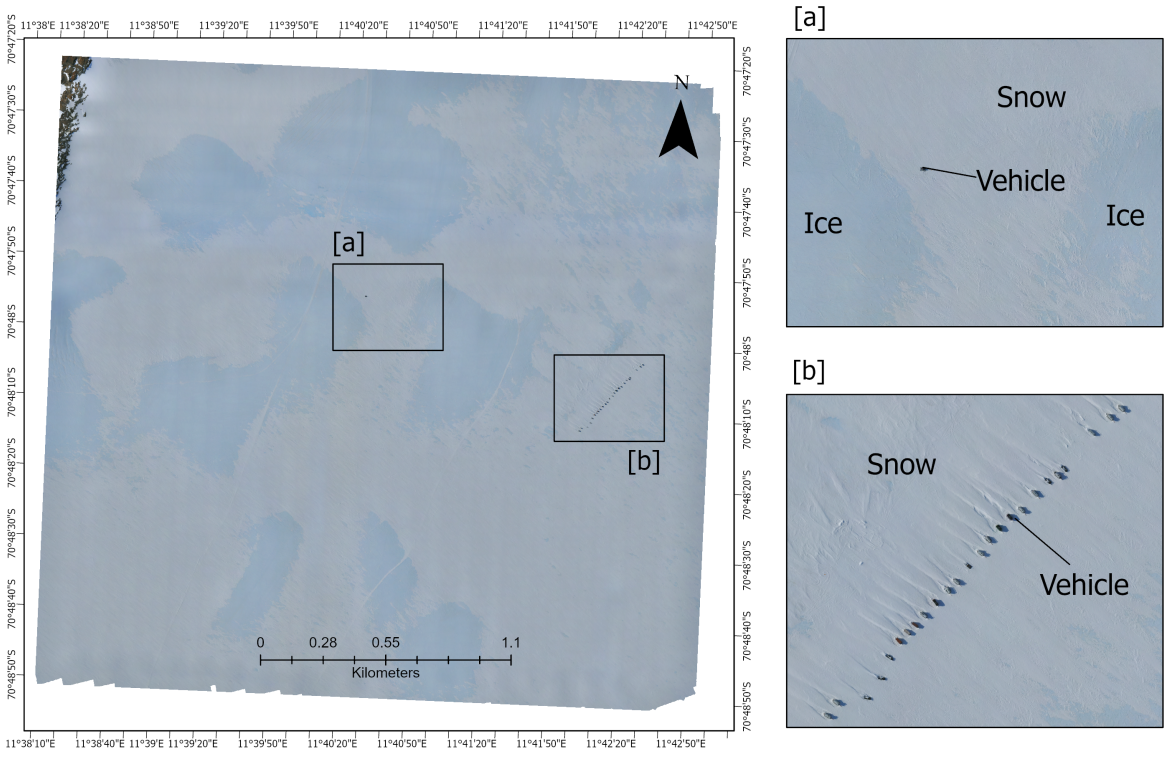

Figure 2: Orthoimage generated from UAV-based survey (right) for 21 Nov 2024 period. Zoomed in view of a) covering the snow, ice, and vehicle, and b) Vehicles and snow-covered area within the surveyed area.

The optical data were classified as either snow-covered or ice-covered using a simple supervised classification algorithm performed in the ArcGIS Pro application. The transition in the classification map ensures the application of the corresponding density values for geodetic mass change estimation. We used a snow density (ρ_{snow} = 300 kg m^{-3}) following Amory et al, (2021), for pixels transitioning from snow to snow or ice with negative elevation change, leading to a melting scenario. Whereas, if a pixel with ice experiences accumulation (positive elevation change) and transit to snow class, then also snow density is used. Only in cases when the ice surface experiences accumulation or ablation and stays in ice class during the transition, an ice density (ρ_{ice} = 917 kg m^{-3}) following (Cuffey and Paterson, 2010) was used. The conditional density selection is performed as given in Eq. (1).

$$\rho_{ij} = \begin{cases} \rho_{snow}\ if\ transition\ is\ snow\ to\ snow\ or\ ice\ and\ \Delta h_{ij} < 0\ (ablation) \\ \rho_{snow}\ if\ transition\ is\ ice\ to\ snow\ and\ \Delta h_{ij} > 0\ (accumualtion) \\ \rho_{ice}\ if\ transition\ to\ ice\ to\ ice\ (ablation\ or\ accumulation) \end{cases} \quad (1)$$

3.3 Elevation-derived Geodetic Mass Change

In this study, ice flux corrections were not applied to the DEM differencing results because reliable surface velocities could not be derived for the study period. Feature tracking on orthoimages was attempted, but pronounced surface changes prevented

https://doi.org/10.5194/egusphere-2025-5601
Preprint. Discussion started: 5 March 2026

robust displacement estimates, and available satellite velocity products were not sufficiently consistent with the evolving surface conditions over the analysed region. It shall be noted that the flow velocities at the study site south of the Schirmacher Oasis are relatively low (~6 m a^{-1}), as the surrounding oasis topography and nunataks act as physical barriers to ice movement (Sunil et al., 2007). These conditions minimize the contribution of horizontal and vertical ice flux divergence to surface elevation changes observed in this region, making the measured elevation changes largely representative of local mass change signals. Therefore, our results represent elevation–derived mass change over the study area, rather than flux-corrected mass-balance estimate.

All the calculations were performed after masking out man-made installations (e.g., AWS, station route/track markers, and antenna/tower) and transient vehicle and their tracks from point cloud to isolate ice sheet surface processes only. All generated DEMs were co-registered, resampled to 0.5m and subtracted from each other to generate pixel wise elevation change (Δh_{xy}) across the study area as shown in Eqn. (2). Next, the pixel wise volume change was calculated as shown in Eqn. (3). Following which the elevation-derived geodetic mass change mc_{geo} (cm w.e.) for different time period was determined as shown in Eqn. (4) using surface transition dependent density.

$$\Delta h_{xy} = h_{DEM2(xy)} - h_{DEM1(xy)} \quad (2)$$

$$\Delta V = \Delta h_{xy} \times A_{pix} \quad (3)$$

$$mc_{geo} = \Delta V \, f_{\Delta v} \quad (4)$$

Where Δh_{xy} is the local surface elevation change (m), ΔV is the volume change (m^3) obtained at each pixel by multiplying area of pixel (A_{pix}) with observed elevation change values. $f_{\Delta V}$ is a density conversion factor adopted from Huss (2013). It was derived using $\rho_{ij}/\rho_w . \rho_w$, where ρ_w is the density of water (1000 kg m^{-3})

3.4 Uncertainty Estimation

There are three uncertainty contributors to geodetic mass change uncertainty $\sigma_{mb_{geo}}$ which includes elevation change uncertainty, density uncertainty, and area uncertainty (Fischer et al. 2015). Since the pixel area (A_{pixel}) is constant across the study domain, its contribution to the propagated elevation-derived geodetic mass change uncertainty was considered negligible. Considering the autocorrelation between DEMs (Rolstad et al., 2009), spatially correlated area (A_{corr}) was estimated, defined by Eqn. (5)

$$A_{corr} = \pi \cdot L^2 \quad (5)$$

https://doi.org/10.5194/egusphere-2025-5601
Preprint. Discussion started: 5 March 2026

Where, L is the decorrelation length of 790 m for flat blue ice or snow area as suggested by Rolstad et al., (2009). Given the study area is larger than A_{corr}, uncertianty of elevation change $\sigma_{\Delta h}$ can be qunatified as shown in Eqn. (6)

$$\sigma_{\Delta h} = SD\sqrt{\mathrm{A_{corr}}/5A} \quad (6)$$

Where *SD* represent the std dev. of the check point vertical residuals for each DEM (Table 2). In the absence of stable, ice-free terrain to estimate random elevation-change errors from DEM differencing, we used checkpoint-derived vertical errors for each DEM as suggested by Gindraux et al., (2017). The vertical error of each DEM pair is propagated to estimate the elevation-change uncertainty.

The volume change uncertainty estimated using Eqn. (7) as follows:

$$\sigma_{\Delta V} = \sigma_{\Delta h} \cdot A \quad (7)$$

The geodetic mass change uncertainty $\sigma_{\mathrm{mc_{geo}}}$ is finally calculated using Eqn. (8)

$$\Delta\mathrm{mc_{geo}} = \sqrt{(\Delta V \cdot \sigma_{f_{\Delta v}}/A)^2 + (\sigma_{\Delta V} \cdot f_{\Delta v}/A)^2} \quad (8)$$

Where $f_{\Delta v}$ is the density conversion factor derived using density raster as given in Eqn. 1. Following Huss (2013) and Engel et al., (2018), the spatially distributed density factor uncertainty $\sigma_{f_{\Delta v}}$ is assumed to be 0.06 and 0.09 for ice and snow, respectively.

4 Results

4.1 UAV DEM and Orthoimage Generation

All the products generated using the SfM-MVS workflow were evaluated. The point cloud accuracy was estimated at checkpoints. Errors presented in Table 2 reflect checkpoint discrepancies derived from independent ground checkpoints that are not involved in model generation; thus, post-control point correction errors represent the final accuracy of the generated point clouds. The corrected point clouds were subsequently used to generate orthomosaics and DEMs. To evaluate spatial accuracy, error metrics were computed for both ground control points (GCPs) and check points. The XY error represents the root mean square error (RMSE) of the horizontal (X and Y) coordinates, while the Z error corresponds to the RMSE of the vertical (elevation) coordinate. These metrics provide a quantitative measure of the georeferencing accuracy achieved during the SfM processing workflow. A summary of the resultant error statistics across all survey dates is presented in Table 2.

https://doi.org/10.5194/egusphere-2025-5601
Preprint. Discussion started: 5 March 2026

250

Table 2. Details of data processing and error metrics such as error in X and Y coordinate, error in Z (vertical) coordinate and error in XY (horizontal) coordinate and total error for the Structure-from-Motion and Multi Stereo View (SfM- MVS) image processing workflow and Ground Check point accuracy over point cloud for different survey dates. All the given errors are in centimetres.

Survey Date	Procedure	X error (cm)	Y error (cm)	Z error (cm)	XY error (cm)	Total error (cm)
17 November 2023	Initial Image Alignment	5.65	7.46	5.03	9.36	10.63
	Post Tie Point Optimization	6.12	8.40	5.43	10.39	11.73
	CP Error	7.71	5.23	6.23	9.23	11.21
3 December 2023	Initial Image Alignment	10.75	14.24	15.56	17.84	23.67
	Post Tie Point Optimization	10.69	12.35	10.85	16.34	19.62
	CP Error	4.55	6.12	8.28	7.63	11.26
17 December 2023	Initial Image Alignment	9.96	13.68	5.92	16.92	17.93
	Post Tie Point Optimization	3.93	3.00	1.33	4.95	5.12
	CP Error	2.99	2.78	5.94	4.08	7.21
21 November 2024	Initial Image Alignment	12.27	11.01	8.97	16.49	18.79
	Post Tie Point Optimization	9.57	5.14	3.73	10.87	11.49
	CP Error	4.47	2.44	3.20	5.10	6.02

255 **4.2 Snow and ice cover transition**

The spatial distribution of the snow and ice cover for sub-seasonal, seasonal, and annual period for both larger and smaller areas is shown in Fig. 3a-e. The snow and ice cover are seen to vary slightly at the sub-seasonal time (Fig. S3a-b) around the elevation intervals 420 - 450 m, while changes in snow cover is most visible between seasonal (Fig. S3c) and annual (Fig. S3d-e). Figure 3 shows the percentage area covered by snow and ice during the respective periods. Across all observation
260 periods, snow consistently covers a larger surface area than ice within the study region. On average, snow accounts for approximately 57–69% of the total area, while ice occupies 30–43%, with the snow-covered fraction being highest during sub-seasonal and seasonal periods and slightly lower during annual scales (Fig. S4).

4.3 Surface Elevation Changes

4.3.1 Sub-seasonal Elevation Change

265 During sub-seasonal 1 period (17 November–3 December 2023), the UAV-derived elevation change showed a mean of +0.004 ± 0.042 m, with values ranging from -0.757 m to +0.499 m (Table 3). Spatially, most surface lowering occurred across the

https://doi.org/10.5194/egusphere-2025-5601
Preprint. Discussion started: 5 March 2026

central and northern, lower-elevation areas (<470 m), whereas slight elevation gains were found around southern higher-elevation zones (>470 m) (Fig. 3a). The elevation change histogram (Fig. 3b) is slightly right-skewed, indicating a greater proportion of negative Δh values. Although within the period, the area experienced significant surface lowering, a larger portion of the area experienced elevation loss. In contrast, during sub-seasonal 2 period (3–17 December 2023), the study area exhibited a net elevation gain, with a mean of +0.012 ± 0.042 m (range: –0.483 m to +1.172 m; Table 2). The elevation change map (Fig. 3) shows a contrasting pattern to that of sub-seasonal 1, with losses (>470 m) concentrated in the western and middle regions. The greatest elevation increase occurs in the northeast above 1 m. Although areas of surface lowering are more spatially extensive, the histogram is slightly left-skewed, indicating that positive elevation changes dominate overall.

The comparison between the two sub-seasonal periods (Fig. 3a and 3c) reveals a clear shift in elevation-change dynamics. During sub-seasonal period 1, lower elevations experience surface lowering while higher elevations undergo surface thickening. In contrast, sub-seasonal period 2 shows the opposite trend, with lower elevations gaining elevation and higher elevations exhibiting surface lowering (Fig. 3). These high-resolution bi-weekly observations capture a transitional phase in surface conditions, which is likely attributed to snow drift driven by wind gust.

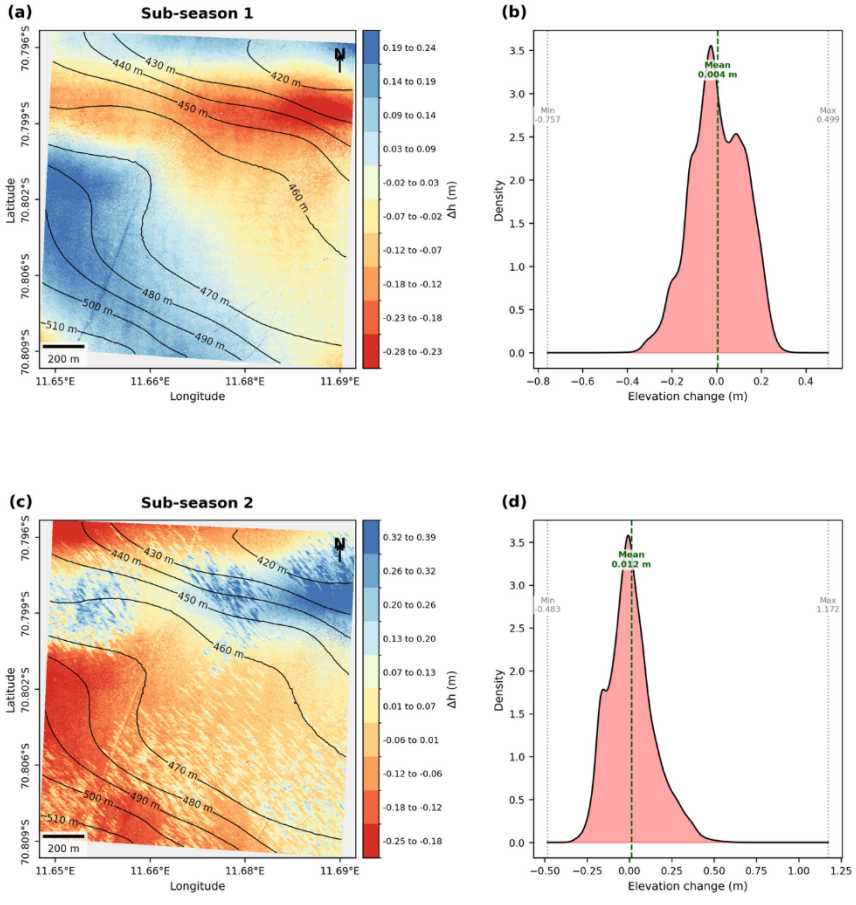

https://doi.org/10.5194/egusphere-2025-5601
Preprint. Discussion started: 5 March 2026

Figure 3. a) Spatial distribution of elevation change, (b) Histogram plot of elevation change density for Sub-seasonal 1 (17 November–3 December 2023), c) Spatial distribution of elevation change, and (d) Histogram plot of elevation change density for Sub-seasonal 2 (3–17 December 2023)

4.3.2 Seasonal Elevation Change

285 During the seasonal period (17 November – 17 December 2023), mean elevation change was +0.007 ± 0.035 m, ranging from –0.434 m to +0.597 m (Table 3). Spatially, a loss of ~0.40 m was recorded at the low-elevation northwestern portion, with contrasting gains in the northeast and mixed changes elsewhere (Fig. 4a). The histogram (Fig. 4b) indicates an overall neutral distribution, while the distribution pattern shows only a slight increase in the low elevation areas < 420m and a negligible change across other elevations. Compared to the bi-weekly sub-seasonal results, these monthly changes highlight the
290 cumulative signals from the short-term elevation changes and processes (Fig. 3a, and 3c).

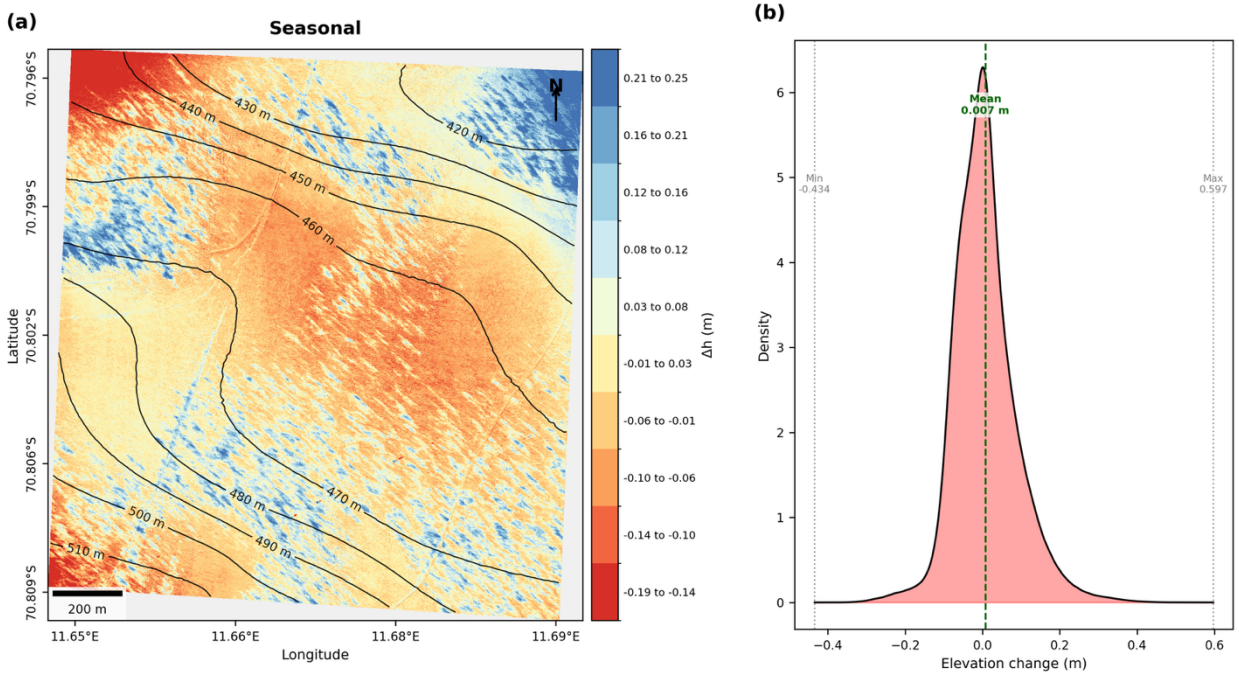

Figure 4: a) Spatial distribution of elevation change, and (b) Histogram plot of elevation change density for the Seasonal period (17 November - 17 December 2023)

4.3.3 Annual Elevation Change

295 Annual elevation change (3 December 2023 – 21 November 2024) was evaluated over two spatial extents: a larger area available only during the annual surveys, and a smaller common extent matching the seasonal/sub-seasonal coverage (Fig. 1). Over the larger area, mean elevation change was +0.023 ± 0.02 m, with values between –1.977 m and +2.360 m (Table 3). The spatial map (Fig. 5a) shows elevation losses concentrated in the mid-western to north-western (lower elevation) portions, and gains towards the east, mostly at flat regions or less than a surface slope of 5 degrees (Fig. S2). The histogram (Fig. 5b) is

https://doi.org/10.5194/egusphere-2025-5601
Preprint. Discussion started: 5 March 2026

300 slightly right-skewed, showing positive mean changes across most elevation bands except 389–409 m and 489–509 m, where the surface slopes were observed to be above 5 degrees (Fig. S2). This indicates that the surface slope is also one of the factors to influence the elevation gain or loss.

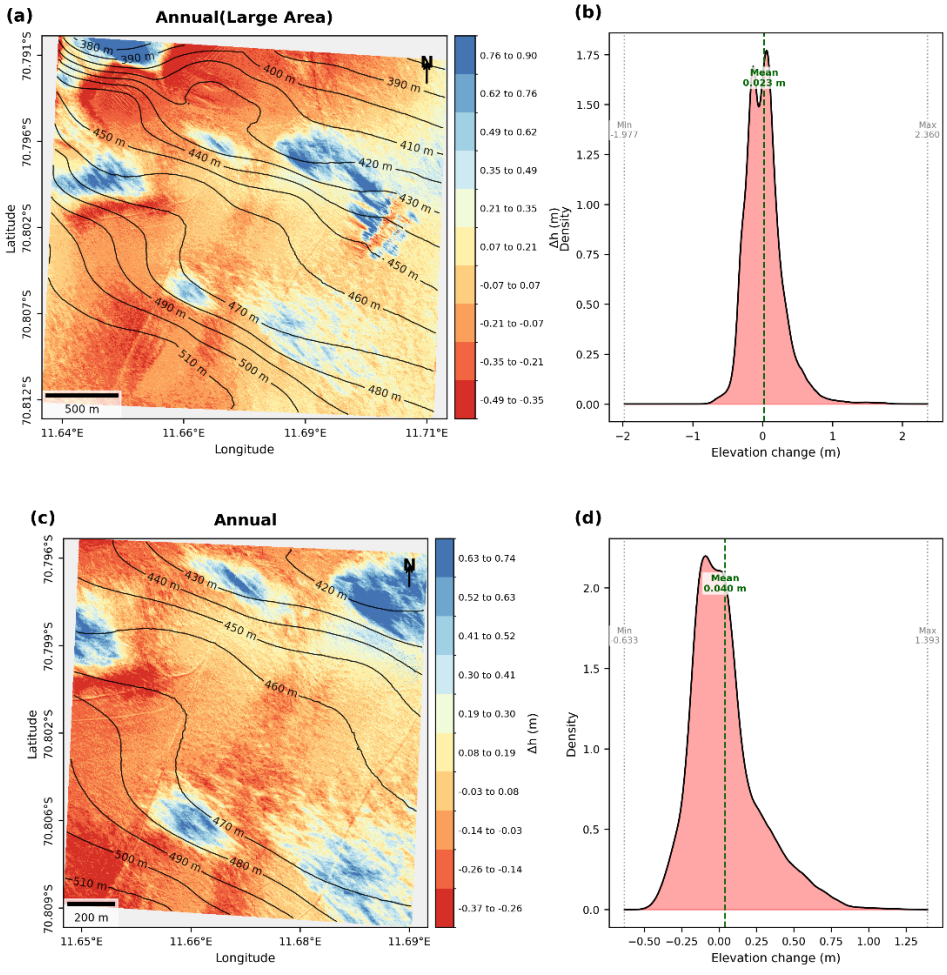

Figure 5. a) Spatial distribution map of elevation change, (b) Histogram plot of elevation change density for the Annual period
305 **(larger area) (3 December 2023 – 21 November 2024). c) Spatial distribution of elevation change, and (d) Histogram plot of elevation change density for Annual period for the seasonal footprint (3 December 2023 – 21 November 2024)**

While analysis of the smaller footprint (Fig. 5c and 5d), suggests elevation loss occurred in most of the surveyed area but at varying levels, the elevation gain is observed as patches. For instance, at southeastern corner, a surface gain was around 0.47 ± 0.036 m was observed between elevation 470m - 480m, where slope ranges from 5-10° (Fig. S1). The largest gains, up to
310 +1.393 ± 0.036 m, mostly encompass at lower elevations below 430m. Whereas losses greater than –0.23 ± 0.036 m were found at higher elevations above 490 m, where surface slope is around 2-5° (Fig. S1, 17 Dec 2023), particularly in the south-western and mid-western parts, while gains are localised as patches observed at the corners of north-east and south-east

https://doi.org/10.5194/egusphere-2025-5601
Preprint. Discussion started: 5 March 2026

directions. These annual patterns emphasise the spatial heterogeneity and their ability to directly influence the surface mass balance in the study area.

315

Table 3: Summary of Surface Elevation Change over different periods with different statistics like mean, minimum value and maximum value and error in metres (m). Units of elevation change are represented in meters over corresponding time intervals.

Period	Duration (days)	Mean (m)	Min (m)	Max (m)	Error (m)
Sub-seasonal 1 (17 Nov–3 Dec 2023)	16	0.004	-0.757	0.499	± 0.042
Sub-seasonal 2 (3–17 Dec 2023)	14	0.012	-0.483	1.172	± 0.042
Seasonal (17 Nov–17 Dec 2023)	30	0.007	-0.434	0.597	± 0.035
Annual (3 Dec 2023–21 Nov 2024) *	354	0.040	-0.633	1.393	± 0.036
Annual – Larger Area (3 Dec 2023–21 Nov 2024) *	354	0.023	-1.977	2.360	± 0.02

Note: Annual periods cover two different spatial extents: the first corresponds to the UAV-surveyed smaller area, the second to a broader region analysed using available data (refer to Fig. 1). All elevation changes reflect surface-level changes after masking non-glacial features (e.g., vehicles, infrastructure). Duration is based on exact calendar days for each pair of DEM acquisitions*

4.4 Geodetic Mass Change

320 The Geodetic Mass Change (hereafter referred as mass change) was estimated for four distinct temporal periods using elevation change and density information. The mass change varied substantially across time periods, ranging from a moderate loss during the sub-seasonal (−0.14 ± 0.19 cm w.e.) and seasonal (−0.14 ± 0.24 cm w.e.) intervals to a pronounced gain during the annual period (2.07 ± 0.68 cm w.e.). Overall, the sub-seasonal 1 and large-area annual periods showed positive mass change values of 0.54 ± 0.22 cm w.e. and 0.75 ± 0.58 cm w.e., respectively, indicating net mass accumulation. Figure 6 shows the bar plot
325 of GMB estimated for all time periods.

https://doi.org/10.5194/egusphere-2025-5601
Preprint. Discussion started: 5 March 2026

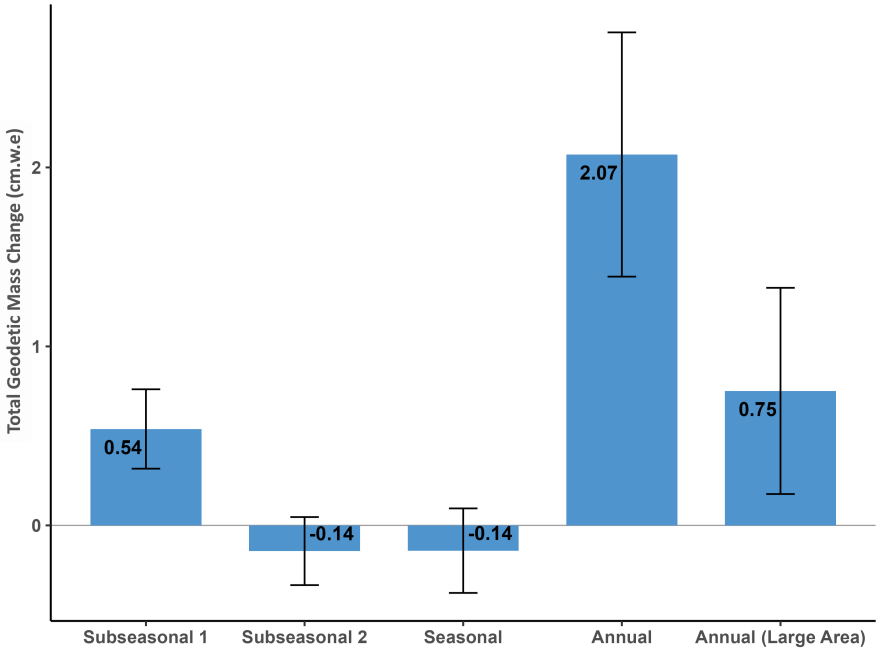

Figure 6. Total Geodetic Mass Change for different temporal periods expressed in centimetres water equivalent (cm w.e). Bars show total mass change values with error bars representing variability across periods.

4.5 Validation

Here, we present a validation of our UAV-derived surface elevation change with in situ stake measurements. While the annual datasets adequately covered all three regions, the reduced spatial footprint during seasonal and sub-seasonal periods constrained further analysis; Therefore, the validation was limited to the annual scale. Three different ablation stakes were found within our study area, which were installed by the Geological Survey of India (GSI), separated by approximately 1.6 km (Fig. 1). The stakes are represented by their unique IDs- GSI 40, GSI 41, and GSI 80.

Surface elevations at the stakes were measured using DGNSS on 03 December 2023 and 21 November 2024, and elevation change (Δh) was calculated from the difference between the two periods. UAV-derived elevations were extracted from DEMs generated for the same dates. The vertical error associated with the stake DGNSS measurements was 0.01 m, while for the UAV DEMs it was 0.07 m. The observed surface elevations at the stake sites are given in Table 4. At all three stakes, both methods consistently indicated surface lowering during 2023–2024, with Δh ranging from –0.17 to –0.39 m. The UAV-derived elevation changes were in close agreement with the stake measurements, with differences of 0.01–0.14 m, which are within the combined uncertainties (Fig. 7).

Furthermore, we estimated the mass change at the stake locations using both UAV derived surface elevation changes and in-situ stake measurements, assuming constant ice density. The comparison shows close agreement across all three stakes,

https://doi.org/10.5194/egusphere-2025-5601
Preprint. Discussion started: 5 March 2026

reflecting similar magnitude and trend as stake-based observations, indicating high consistency between both method and reliability of UAV for mass balance estimation.

Additionally, to evaluate how stake-based distributed mass change estimates perform relative to the UAV-derived estimates, a supplementary analysis was conducted (Section S2). The finding reveals that stake based interpolation approach fails to capture the spatial heterogeneity in mass balance. Consequently, we emphasize that stake network should consider integrating UAV based observation to enhance the spatial distribution and accuracy of mass balance assessments.

Table 4: Details of elevation change collected at three stake locations within the UAV surveyed area and corresponding UAV-based elevation change and mass change estimates

Stake Name	Δh (Stakes, m)	Δh (UAV, m)	Geodetic Mass Change (Stakes, m.w.e.)	Geodetic Mass Change (UAV, m w.e.)
Vettaiya (GSI 40)	-0.248 ± 0.01	-0.390 ± 0.01	-0.227 ± 0.017	-0.358 ± 0.068
Sankalp (GSI 41)	-0.306 ± 0.01	-0.318 ± 0.01	-0.092 ± 0.031	-0.095 ± 0.038
AWS (GSI 80)	-0.205 ± 0.01	-0.171 ± 0.01	-0.061 ± 0.021	-0.051 ± 0.027

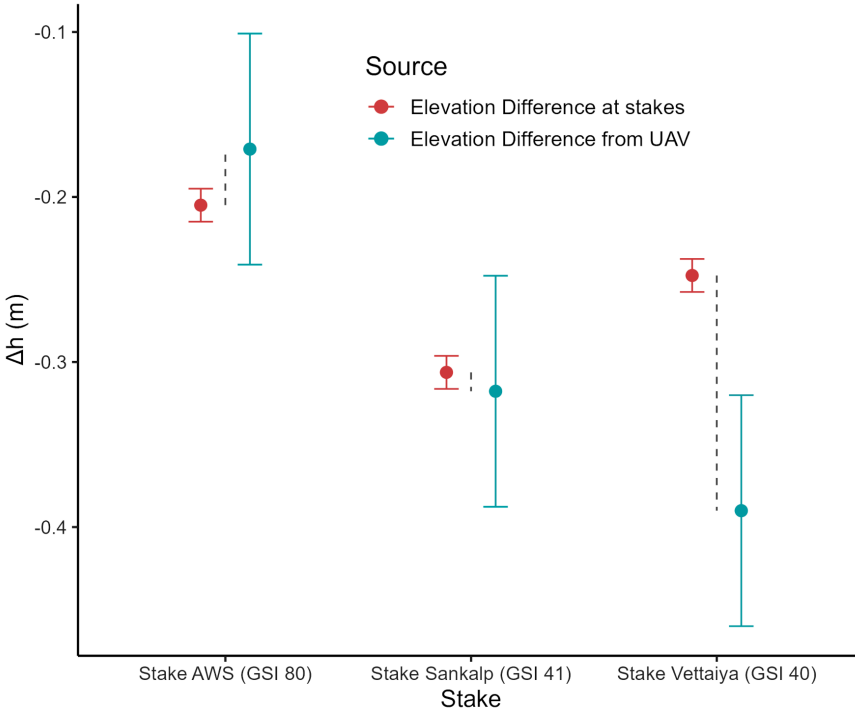

Figure 7: Plot of elevation difference observed at three stake locations and UAV-based estimates.

https://doi.org/10.5194/egusphere-2025-5601
Preprint. Discussion started: 5 March 2026

5 Discussions

5.1 Contribution of Snow and Ice to UAV-derived Geodetic Mass Change Estimates

By leveraging the high-resolution UAV-generated ortho images and DEMs, the study was able to distinguish the snow and ice region in the surveyed area. Thus, mass change was estimated for differing densities based on surface characteristics (snow or ice).

Across all periods except the annual, snow consistently covered more than 67% of the surface area, indicating a predominantly snow-covered landscape with little variability over sub-seasonal to seasonal timescales (Fig. S5, Table 5). In contrast, during the annual period, snow cover drops to 57%, while ice cover increases to 43%. This shift suggests a net transition from snow to ice over the year, likely driven by snow melt, wind redistribution, or compaction due to melting and refreezing.

The contribution of snow and ice to mass change is highly disproportionate to their surface area coverage and varies markedly over time (refer to supplementary Fig. S3b). In sub-seasonal 1, ice accounts for over 90 % of the mass change contribution despite covering only ~31 % of the area (refer to supplementary Fig. S3a), indicating that relatively small ice-covered regions can have a significant influence on mass balance. This dominance then shifts in sub-seasonal 2 and the seasonal period, during which snow becomes the primary contributor −0.74 ± 0.41 cm.w.e. (55.3%), −0.53 ± 0.41 cm.w.e. (57.7%), respectively (Fig. S3a, Table 4), reflecting influence of the changes in meteorological forcing that temporarily favour snow-driven processes.

At the annual scale, however, the control reverts to ice (1.28 ± 0.63 cm.w.e.(61.7%)), even though snow still covers 38.3% of the surface area, suggesting that the long-term (annual) mass balance is governed more by physical processes acting on the ice surface than by seasonal variations in snow cover. These alternating patterns emphasise that temporal mass change variation is not merely associated with shifts in magnitude but reflects changes in the dominant physical processes, and the nature of ice sheet surface cover (ice/snow/firn). This highlights the potential of high-resolution UAV data products at varied time scales for understanding the dynamic nature of surface mass balance in this transition zone.

Table 5: Snow and ice coverage area (in %) with corresponding mass change estimates and associated uncertainty for Sub-seasonal 1, 2, Seasonal, and Annual periods.

Period	Snow Area (%)	Ice Area (%)	Snow Geodetic Mass Change (cm w.e.) ± uncertainty *(contribution to total Geodetic Mass Change)*	Ice Geodetic Mass Change (cm w.e.) ± uncertainty *(contribution to total Geodetic Mass Change)*
Sub-seasonal 1	69	31	−0.06 ± 0.12 *(9.3%)*	0.60 ± 0.34 *(90.7%)*
Sub-seasonal 2	68	32	0.60 ± 0.22 *(44.7%)*	−0.74 ± 0.41 *(55.3%)*
Seasonal	70	30	0.39 ± 0.18 *(42.3%)*	−0.53 ± 0.41 *(57.7%)*
Annual	57	43	0.79 ± 0.05 *(38.3%)*	1.28 ± 0.63 *(61.7%)*
Annual (Large Area)	58	42	0.68 ± 0.07 *(90.7%)*	0.07 ± 0.51 *(9.3%)*

https://doi.org/10.5194/egusphere-2025-5601
Preprint. Discussion started: 5 March 2026

5.2 Influence of density on UAV-derived Geodetic Mass Change Estimates

To evaluate the influence of density on mass change estimates, three scenarios were tested across different timescales: (i) spatially classified snow- and ice-densities (this study), (ii) uniform snow density (300 kg m^{-3}), and (iii) uniform ice density (917 kg m^{-3}). For each case, mass change was calculated in cm w.e. with associated uncertainties.

The sub-seasonal and seasonal mass change observations revealed notable contrasts with scenario-based estimates (Fig. 8). In the first sub-seasonal period, the actual mass change *(based on spatially distributed density)* indicated a net gain of +0.54 cm w.e., closely matched by the "All Ice" scenario (+0.41 cm w.e.), while the "All Snow" scenario (+0.14 cm w.e.) underestimated accumulation. In the second sub-seasonal period, a slight net loss was observed (–0.14 cm w.e.), whereas constant density scenarios show gains, highlighting limitations of simplified snow- or ice-only assumptions. Similarly, the seasonal SMB reflected a loss (–0.14 cm w.e.), contrasting with constant density scenario gains of +0.21 cm ("All Snow") and +0.65 cm ("All Ice"). On an annual scale, mass change (+2.07 cm w.e.) for footprint similar to that of sub-seasonal and seasonal periods fell between the "All Snow" (+1.21 cm) and "All Ice" (+3.71 cm) estimates, with ‘All snow’ scenario exhibiting larger uncertainties and ‘All ice’ assumptions yielding more constrained estimates. For the larger footprint, this study exhibited a mass change of +0.75 cm w.e. which aligns well with ‘All Snow’ scenario (+0.70 cm w.e.) but varies a lot with ‘All Ice’ scenario (+2.14 cm w.e.). This experiment highlights that mass change estimates are highly sensitive to spatial distribution of surface density assumptions.

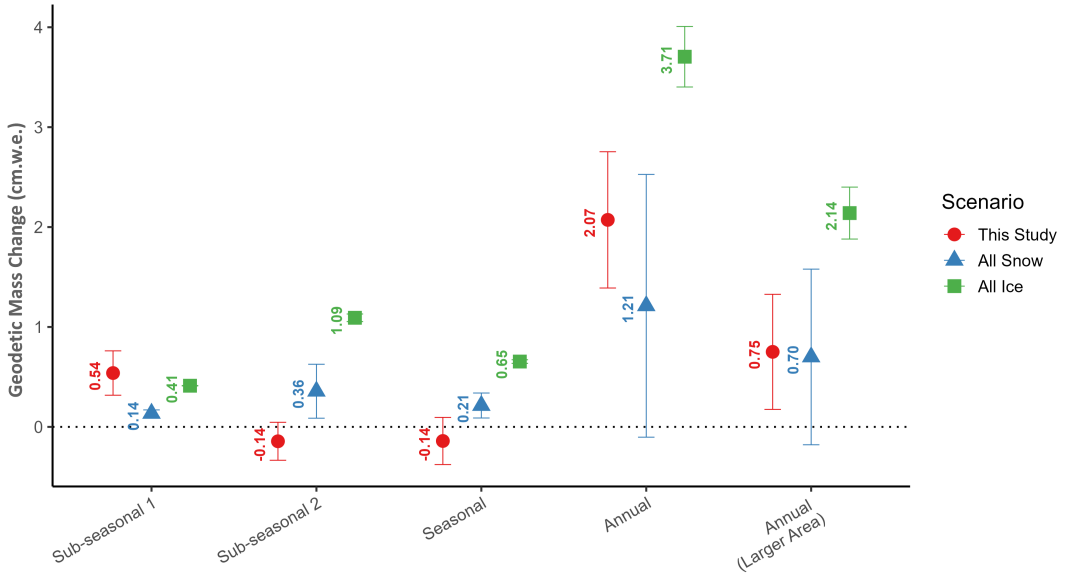

Figure 8. Plot of Geodetic Mass Change estimates to ice and snow surface density assumptions across different periods.

https://doi.org/10.5194/egusphere-2025-5601
Preprint. Discussion started: 5 March 2026

5.3 Impacts of Surface Topography Parameters on UAV-derived Geodetic Mass Change estimates

This section attempts to understand the influence of topographical parameters by leveraging the availability of high-resolution DEM in the study area. The DEM parameters include slope, aspect, and curvature extracted from the UAV-generated DEMs. The study attempts to understand the mass change based on surface slope and aspect for different periods that share the same footprint.

5.3.1. Influence of Slope

To understand the influence of surface terrain slope on mass change across sub-seasonal, seasonal, and annual timescales refer to the Fig. 9. Each circle in the Fig. 9 represents a slope class plotted against its class area contribution (%) on the x-axis and mean mass change (cm w.e.) on the y-axis. The circle size denotes the magnitude of |Geod. Mass Change|, while the color differentiates the four time periods: Sub-seasonal 1 (blue), Sub-seasonal 2 (green), Seasonal (orange), and Annual (red). The symbols correspond to slope classes: circles (0–2°), squares (2–5°), diamonds (5–10°), upward triangles (10–20°), and inverted triangles (>20°). The horizontal grey line indicates equilibrium (zero mass change).

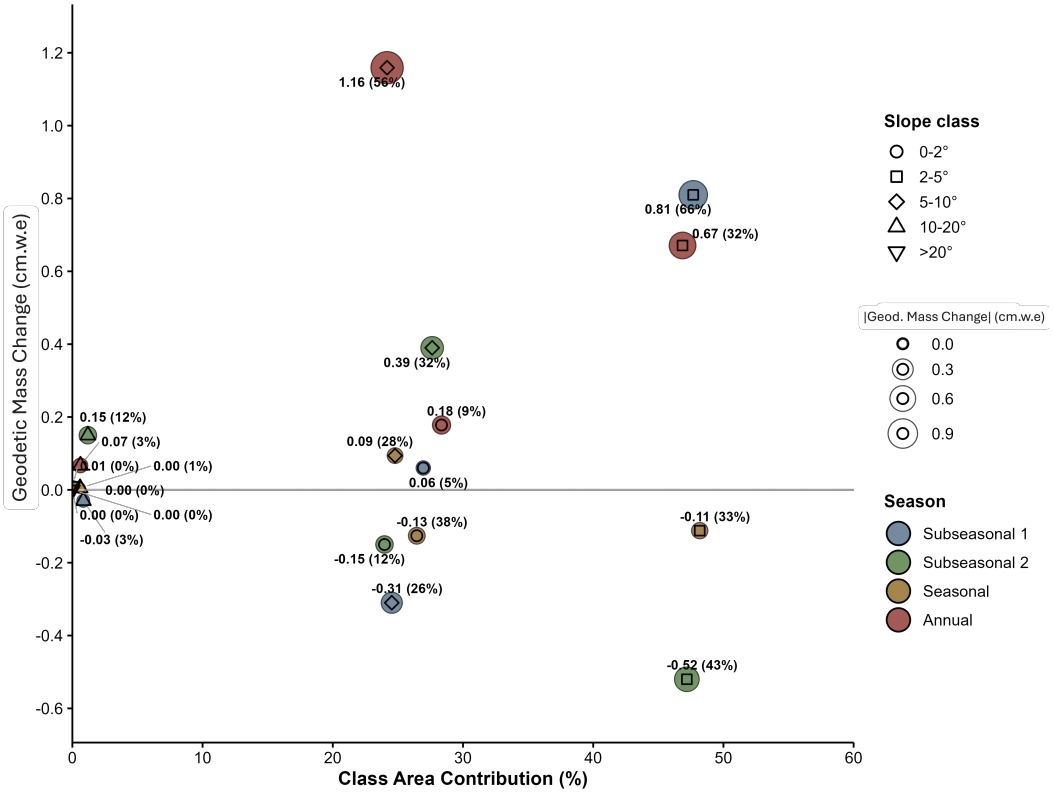

Figure 9: Plot demonstrating the relationship between the surface slope and geodetic mass change across sub-seasonal to annual timescales.

https://doi.org/10.5194/egusphere-2025-5601
Preprint. Discussion started: 5 March 2026

During sub-seasonal 1, the 2–5° class, represented by blue squares in Fig. 9, exhibited the highest mass change (0.81 cm w.e.) and contributed 66.5 % of the total mass balance while covering nearly half of the glacierized area, that is, 47.7 % (Table S1). This indicates that during this period, that is, the early summer season, precipitation preferentially occurs on moderately inclined surfaces that efficiently trap drifting snow. In contrast, the 5°–10° class (blue diamonds in Fig. 9) recorded a negative mass change (–0.31 cm.w.e., 25.7 % contribution), suggesting localized melt or reduced snow retention at steeper gradients even during the early summer phase. Flatter areas (0–2°, blue circles in Fig. 9) showed only a minor gain in mass change (0.06 cm.w.e., 5.2%), likely due to limited topographic shading and potential surface runoff. The steeper slope classes (10–20° and > 20°, blue triangles and inverted triangles in Fig. (9) contributed negligibly, underscoring that high-angle terrain provides minimal storage capacity for seasonal accumulation of snow.

Interestingly, a reversal occurred in sub-seasonal 2, when the glacier experienced a negative mass change but varied at different surface gradients. The 2–5° slopes (green square in Fig. 9) covered the largest portion of the area (47.2 %) but exhibited a negative mass change (–0.52 cm w.e., 43.1 % contribution), confirming that mid-slopes dominate mass loss, while it was mass gain during sub-seasonal 1 period. Meanwhile, the 5–10° class (green diamond in Fig. 9) showed positive mass change (0.39 cm w.e., 32.1 % contribution), reflecting a snow drift event that might have occurred to temporarily accumulate in sheltered or shaded regions as local melting subsided. The flatter (0–2°) and steeper (>10°) slopes maintained marginal values (between –0.15 and +0.15 cm.w.e.), suggesting reduced sensitivity to short-term variations in snow deposition and melt processes during this period.

In the seasonal average, the mass change values approached equilibrium across most slope classes. Flatter (0–2°, represented as orange circles in Fig. 9) and gentle (2–5°, represented as orange squares in Fig. 9) surfaces together accounted for more than 80 % of the glacier area and contributed roughly 70 % of the total mass change. Their mass change estimates showed a minor loss (–0.13 to –0.11 cm w.e.), indicating a near-balanced condition. The 5–10° class (orange diamond in Fig. 9) maintained a slight positive mass change (0.09 cm w.e., 28 % contribution), showing that moderate slopes still favour a minor gain during this transitional phase. Steeper slopes above 10° (orange triangle and inverted triangle in Fig. 9) contributed less than 2 % of the total mass change, reinforcing their limited influence on mass change loss or gain, as they contribute a smaller surface area than other classes (Table S1).

At the Annual scale, mass gain was observed to be greater over mid-slopes. The 5–10° class (red diamond in Fig. 9) displayed the highest mass change (1.16 cm w.e., 55.9 % contribution), even though it represented only 24 % of the total study area. This pattern indicates snow retention and redistribution toward moderately sloped terrain over the entire mass-balance year. The 2–5° slopes (red square in Fig. 9) followed with 0.67 cm w.e. and 32.4 % contribution, while the 0–2° class (red circle in Fig. 9) showed a small positive mass change (0.18 cm w.e., 9 % contribution). Given their smaller coverage area, the steeper slopes (10–20°) contributed marginally (0.07 cm w.e., 3.2 %), and the > 20° class showed no contribution.

Overall, Table S1 and Fig. 9 demonstrate that the slope gradient exerts control on the mass change. Gentle to moderate slopes (2–10°) consistently emerged as the primary zones, exhibiting the highest mass change magnitude and spatial contribution across all timescales. The shift in mass loss and gain between sub-seasonal 1- and 2-time scales is reflected in the seasonal

https://doi.org/10.5194/egusphere-2025-5601
Preprint. Discussion started: 5 March 2026

timescale, which led to a minor gain over the study area. The key inference is that 5-10° has relatively less area coverage than 2-5° (Table S1 and surface slope in Fig. S1) and plays an important role in the mass change interplay at various time scales, as shown in Fig. 9 and Table S1. Both flatter and steeper terrains showed limited contributions, which may be due to surface runoff at flat terrains and direct exposure to sunlight during the summer season, leading to inefficient trapping of drifted snow. The persistent dominance of mid-slopes across sub-seasonal, seasonal, and annual periods underscores their critical role in sustaining positive annual mass change.

5.2.2. Influence of Aspect

During sub-seasonal 1, a strong directional asymmetry was observed. Figure 10 shows the relationship between the mass change and terrain aspect. Figure 10a highlights the southern and western aspects, with relatively small mass change and area contributions (bottom panel). Each circle represents an aspect class plotted against its class area contribution (%) on the x-axis and the mean mass change (cm w.e.) on the y-axis. The circle size denotes the magnitude of |Geodetic Mass Change|, while the color differentiates the four time periods: Sub-seasonal 1 (blue), Sub-seasonal 2 (green), Seasonal (orange), and Annual (red). The symbols correspond to the aspect classes: circles (north), squares (northeast), diamonds (east), upward triangles (northwest), inverted triangles (southeast), crosses (south), diagonal crosses (southwest), and asterisks (west). The horizontal grey line indicates equilibrium (zero mass change). The Northeast (NE, blue square in Fig. 10a) aspect recorded the highest mass change of 0.77 cm w.e., contributing 51 % of the total mass change while covering only 20 % of the total study area (Table S2). The East (E, blue diamond in Fig. 10a) also showed a positive mass change (0.23 cm w.e., 15.6 %) despite a small area fraction (6 %). In contrast, the northern region (N, blue circle in Fig. 10a) exhibited a negative mass change (–0.34 cm w.e.) but still accounted for 22% of the total contribution owing to its extensive coverage (54%) (Fig. 10a). The Northwest (NW, blue triangle in Fig. 10a) had a small negative balance (–0.13 cm w.e., 8.6 %), whereas the southern aspects (SE inverted triangle, S with cross, SW with diagonal cross, W with asterisks symbols all in blue color in Fig. 10b, right panel) contributed less than 2 % each, with near-zero mass change values, respectively. This suggests that early season accumulation is preferentially focused on the northeastern and eastern slopes, likely because of the prevailing wind direction observed in the study area.

In sub-seasonal 2 (Fig. 10a, green symbols), the pattern reversed, with the North aspect region (N, green circle in Fig. 10a) showing a positive mass change (0.64 cm w.e., 31.7 %), while the Northeast (NE, green square) showed a negative (–0.64 cm w.e.) but still contributed 31.7 %. This clear switch between the N and NE aspects may reflect the direction and intensity of solar radiation over the season, which influences local melt and accumulation patterns (predominantly snow drifted due to strong wind gusts) according to the slope's orientation relative to the sun. The Northwest aspect region (NW, green triangle in Fig. 10) mass change estimates showed a positive (0.28 cm w.e., 13.8 %) value. Meanwhile, the East (E, green diamond in Fig. 10a) and Southeast aspect regions (SE, green inverted triangle in Fig. 10b) exhibited negative mass change values (–0.30 and –0.10 cm w.e.) and modest contributions (<15 %). Other aspects, such as the southern and western sectors (S in cross, SW in diagonal cross, W in asterisks, all in green, as shown in Fig. 10b), remained almost inactive, contributing less than 3% each.

https://doi.org/10.5194/egusphere-2025-5601
Preprint. Discussion started: 5 March 2026

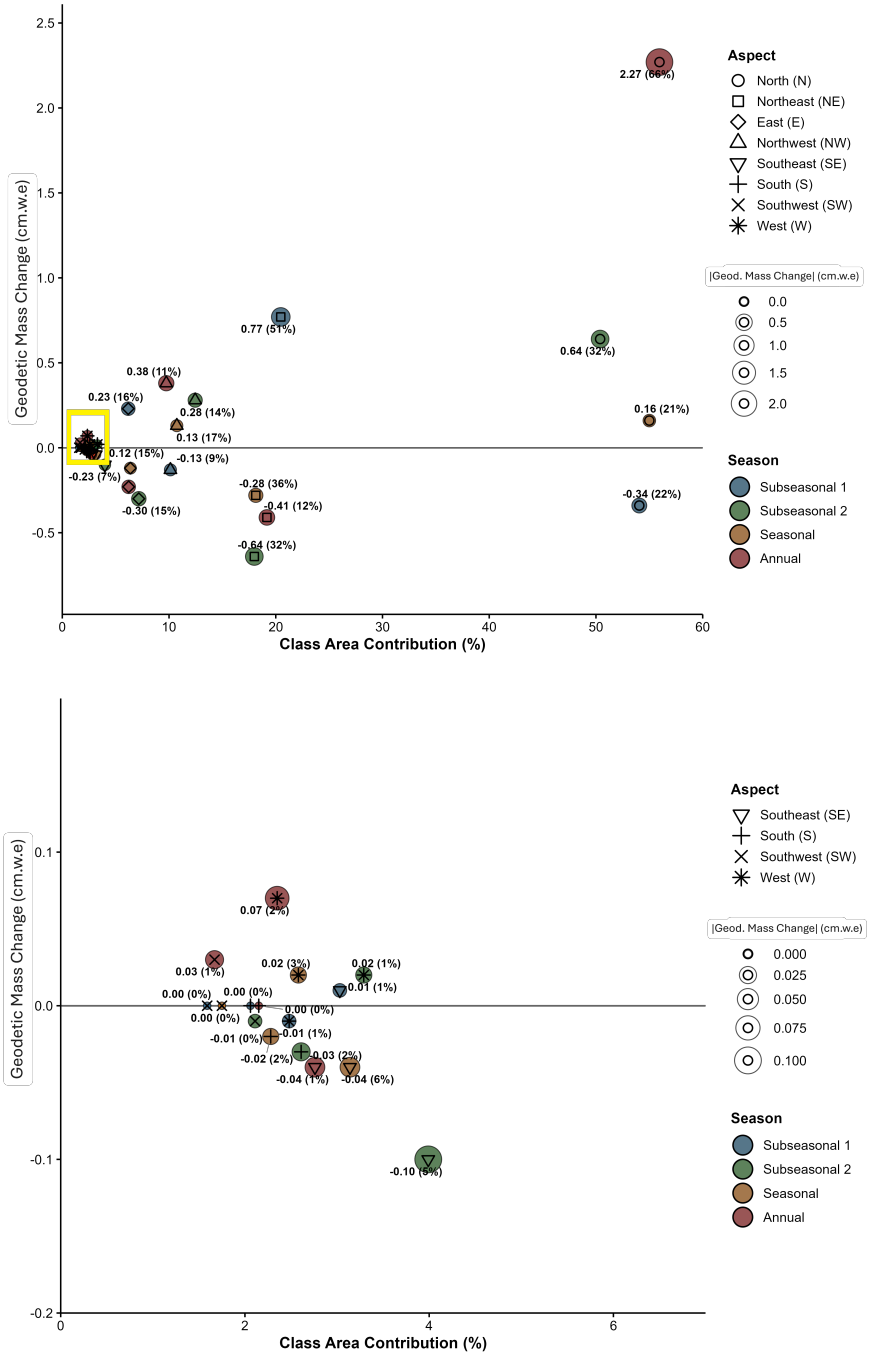

Figure 10 (a) Plot demonstrating the relationship between surface aspect and geodetic mass change across sub-seasonal to annual timescales (top panel). Plot representing a zoomed-in view of (highlighted in yellow box) in Figure 10b (bottom panel).

https://doi.org/10.5194/egusphere-2025-5601
Preprint. Discussion started: 5 March 2026

At the seasonal scale (Fig. 10a, orange symbols), the mass change values approached equilibrium. The North aspect region (N, orange circle in Fig. 10a) maintained a slightly positive mass change (0.16 cm w.e.) with a 20.7 % contribution across 55 % of the glacier area (Table S2). The Northeast (NE, orange square in Fig. 10a) and East (E, orange rectangle in Fig. 10a) regions exhibited lower negative mass changes (–0.28 and –0.12 cm w.e.), yet together they contributed over 50% of the total mass change. The Northwest aspect (NW, orange triangle in Fig. 10a) indicated a small positive mass change (0.13 cm w.e., 17.2 %), confirming that the northern orientations remain the study area's active mass-gaining zones. In contrast, the southern (S, orange cross in Fig. 10b) and western (SW in diagonal cross, W in asterisks, both in orange color in Fig. 10b) aspects remained near neutral, contributing less than 6 % of the total combined mass change.

At the annual scale (Fig. 10a, red symbols), a pronounced contrast was observed compared to the other sub-seasonal and seasonal periods. The northern aspect (N, red circle in Fig. 10a) showed a dominant positive mass change (2.27 cm w.e.) and the highest contribution (66 %) while occupying 56 % of the glacier area. This demonstrates that north-facing slopes are primarily responsible for mass-gain zones throughout the year. The Northwest (NW, red triangle in Fig. 10a) also exhibited a positive mass change (0.38 cm w.e., 11 %), indicating sustained drifted snow preservation in shaded terrain. Meanwhile, slope aspects such as the northeast (NE, red square in Fig. 10a) and east (E, red diamond in Fig. 10a) exhibited negative mass change (–0.41 and –0.23 cm w.e., respectively), indicating increased surface melting due to stronger solar exposure. The southern (red cross in Fig. 10b) and western (red asterisks in Fig. 10b) aspects maintained near-zero or slightly negative mass change values (–0.04 to 0.07 cm w.e.) and collectively contributed less than 3 % of the total. While the Southwest aspect (red diagonal cross in Fig. 10b) showed a minor positive mass change of 0.03 cm w. e., the remaining aspects showed a meagre contribution to the mass change owing to their limited area coverage in the study area.

Overall, our analysis demonstrates that aspect exerts a strong control on mass change spatial variability. Positive mass change is concentrated on the north-to northeast-facing slopes, whereas south- and west-facing slopes remain melt-dominated across all time periods. This directional asymmetry, consistent from sub-seasonal to annual scales, emphasizes the influence of solar radiation exposure, shading geometry, and local microclimate on the mass change distribution within the study area.

5.3 Climatic Variables and Geodetic Mass Change

The transition from mass gain during sub-seasonal 1 to sub-seasonal 2 appears closely linked to changes in temperature, wind chill, and wind gust. Between November and December 2023, a rise in temperatures and gusty winds at the study site promoted snow drifting, resulting in localized mass change changes between sub-seasons 1 and 2. We analyzed daily averages of temperature, wind chill, and maximum wind gusts recorded at Automatic Weather Station (AWS) near the Maitri Station (Fig. 11) as well as precipitation measurements. The trend indicates that temperatures increased during November -December with the onset of the summer season. The maximum wind gust varied every day within the range of 10-50 Knots. Although the wind chill during November-December showed an increasing trend, it had high variations on a daily scale. The precipitation gauge recorded trace snowfall on 25th, 28th, and 29th of November, with 0.2mm snowfall on 26th. During December, snowfall

https://doi.org/10.5194/egusphere-2025-5601
Preprint. Discussion started: 5 March 2026

was recorded during 8th (2.3mm), 9th, 10th (1mm), 12th (0.1mm), 19th, 20th (0.5mm), 22nd, 24th and 25th (0.1mm). These short-term variations in climatic variables such as temperature, wind chill, and wind gust and snowfall have a crucial role in regulating sub-seasonal to seasonal mass balance of ice sheet, which has also been previously noted in some studies around Dronning Maud Land (Birnbaum et al., 2010; Thiery et al., 2012). During sub-seasonal 2, surface mass gain might be supported by multiple episodes of snowfall. Sustained gusts of up to ~50 knots primarily flowing in the direction toward the northwest from South-east, contributed to snow redistribution. This effect is evident in Fig. 6 & 7, where the lower-elevation northeast region (~450 m and below) gained mass in sub-seasonal 1 but experienced mass loss in sub-seasonal 2. The longer duration of gust events in sub-seasonal 2 (~8–9 days) compared to two shorter peaks in sub-seasonal 1 further amplified snow drift and its impact on mass change.

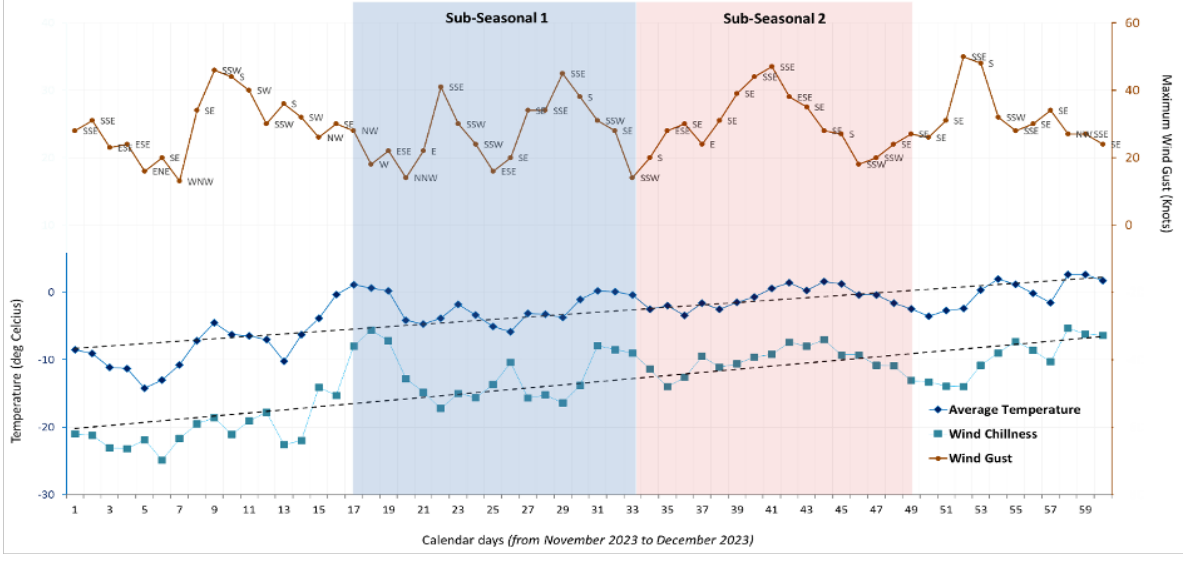

Figure 11: Plot of daily average temperature, wind chillness and maximum wind gust recorded in Maitri station for the months November and December 2023. Blue box indicates periods Sub-seasonal 1 and red indicates Sub-seasonal 2.

On the annual scale (November 2023–November 2024), temperature trends remained largely consistent with temperatures ranging from -45C to +5C (Fig. 12), with wind chill showing a similar pattern. Wind gusts peaked at ~100 knots in July 2024, when temperatures were relatively lower, highlighting that the combined influence of gusts, temperature and snowfall can alter the surface mass balance at an annual scale. The negative surface mass balance over the study area at the annual scale could be linked to overall surface melt (Winther et al., 1996), sub-surface melt (Sinharay, 2022), snow sublimation by strong katabatic winds or removal or erosion of snow due to wind redistribution (Birnbaum et al., 2010; Thiery et al., 2012). In contrast, the positive surface mass balance could be explained by long-term snow accumulation over the slopes of ice sheets. The snow distribution pattern or snow ridges over the study area can be well explained with the direction of wind flow (Fig. 12). Overall, these observations indicate that sub-seasonal and seasonal mass change variability is strongly influenced by the

https://doi.org/10.5194/egusphere-2025-5601
Preprint. Discussion started: 5 March 2026

interplay of fluctuating temperature, wind chill, and gust events, at a daily scale which drives snow drift and alter surface mass distribution, whereas annual trends smooth out these short-term fluctuations.

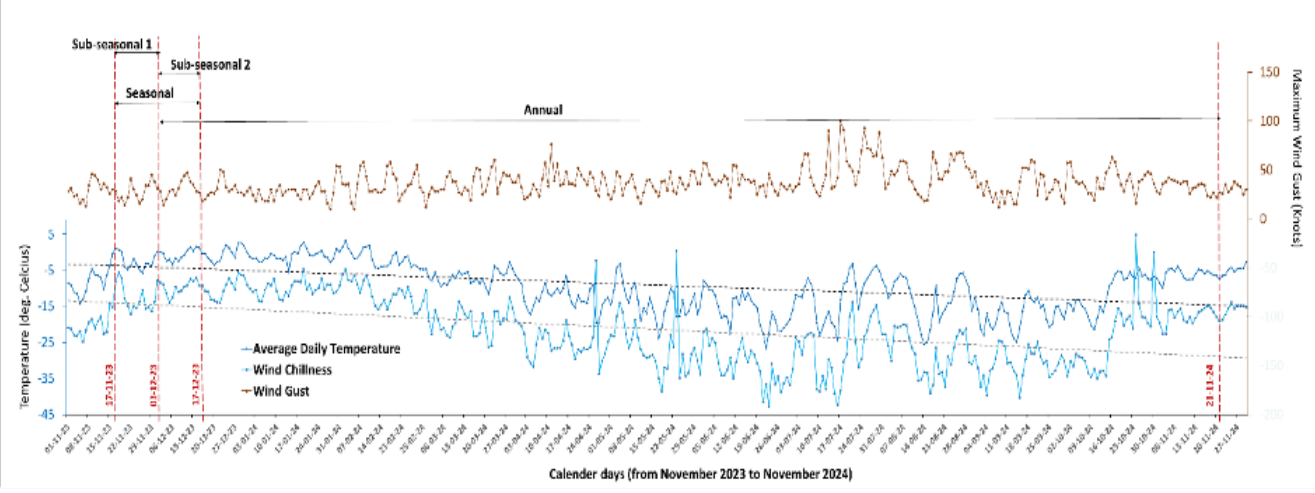

Figure 12: Plot of daily average temperature, wind chillness and maximum wind gust recorded in Maitri station from November 2023 to November 2024. The linear trends of Average daily temperature and wind chillness are shown in dotted black lines. The vertical red lines indicate the UAV surveying time stamp (date is denoted in red font) and the double arrows between vertical red lines represent the respective periods such as Sub-seasonal 1, Sub-seasonal 2, Seasonal, and Annual where geodetic mass change were estimated.

5.4 Field Challenges and Recommendations

Deploying UAVs in Antarctic glacier environments presents a unique set of challenges due to the extreme environmental conditions, logistical complexities, and technical constraints inherent to polar fieldwork. Addressing these issues is critical to ensuring successful data collection and maximizing the scientific value of UAV surveys.

One of the most significant environmental challenges is the extreme cold, which severely affects UAV battery performance and sensor reliability. Batteries tend to drain rapidly at sub-zero temperatures, often reducing effective flight times to less than half of what is typical in temperate conditions. To mitigate this, we recommend storing batteries in insulated containers, pre-warming them before flight, and using heating pads or chemical warmers if necessary. Limiting flight duration and flying during the warmest part of the day can also improve battery longevity. Wind conditions pose another major obstacle. Antarctic field sites frequently experience high winds and sudden gusts, which can compromise flight stability and even lead to mission failure or UAV loss, therefore, it is essential to conduct UAV operations during low-wind periods, ideally when wind speeds are below 5-8 meters per second (10-15 Knots as higher turbulence can introduce instability and increase point-cloud co-registration errors. Real-time weather monitoring using automatic weather stations or satellite-based forecasts should be integrated into daily flight planning.

https://doi.org/10.5194/egusphere-2025-5601
Preprint. Discussion started: 5 March 2026

Snow surface homogeneity presents additional difficulties for photogrammetric processing. UAV images of flat, featureless snowfields often lack sufficient contrast, which leads to poor image matching and unreliable digital surface models (DSMs). This issue can be mitigated by deploying artificial ground control points (GCPs) with high-contrast markings, or by using UAVs equipped with LiDAR sensors, which are not affected by surface texture. In areas where visual navigation is impaired by white-out conditions, reliance on GPS waypoint missions and high-precision georeferencing (e.g., RTK or PPK GNSS) is essential, as manual line-of-sight flying may be unsafe or infeasible. Technically, UAVs used in Antarctica must balance payload capacity with portability. Limited payloads restrict the types of sensors that can be used such as thermal, hyperspectral, or LiDAR sensors, which may exceed the capacity of small multirotor platforms. Selecting UAV platforms with modular sensor bays or hybrid designs (e.g., fixed-wing vertical take-off landing-VTOLs) can improve both endurance and sensor flexibility. Some of the recommended configuration of UAV for polar environments are given in Table.6. The setup of RTK or PPK base stations, necessary for precise geolocation, can be logistically difficult in remote and crevassed terrains. When possible, using pre-surveyed geodetic benchmarks or integrating base data from nearby GNSS stations can help address this challenge.

Table 6: Recommended configuration of UAV for Antarctica or other polar environments

Property	Specification	Use Case / Purpose
Takeoff / Landing system	Fixed-wing UAV with vertical take-off and landing (VTOL); no runway required	Enables deployment from confined areas such as ships or nunataks
Flight endurance	> 60 minutes (preferably up to 180 minutes)	Facilitates extended aerial coverage for large-area surveys
Operating temperature range	-15 °C to +50°C (or as required)	Ensures UAV functionality in extreme cold or variable climate conditions
Communication range	> 10 km	Ensures control and data transmission over wider operational zones
Wind resistance	> 20 m/s	Capable of stable flight in harsh and gusty Antarctic wind conditions
Payload compatibility	Modular / Flexible	Supports integration of various mission-specific sensors
Fuel type compatibility	Battery-powered and/or liquid fuel capable	Allows optimization of energy source based on endurance and logistical requirements
Weight class	Flexible, based on mission needs	Accommodates various payload and endurance trade-offs
Navigation system	GNSS + RTK/PPK support	Allowing high-precision georeferencing for the mission
Autonomous capabilities	Pre-programmed mission with detailed security procedures e.g., obstacle avoidance and return-to-home	Reduces the need for constant manual control and improves the security of the UAV
Environmental protection & transportation	Foldable or modular design for easy assembly, yet IP-rated (IP67)	Allows rapid deployment with protection against snow and drizzle.

https://doi.org/10.5194/egusphere-2025-5601
Preprint. Discussion started: 5 March 2026

5.5 Limitations of the Study and Future Scope

While this study highlights the potential of UAVs in resolving fine-scale (cm-level) surface processes in Antarctica, we acknowledge certain limitations. The area surveyed is confined to a relatively small area, due to battery limitations, which limits the ability to relate our results to broader Antarctic surface processes. The findings, therefore, remain highly localised. Though our approach explicitly accounted for pixel-wise density allocation to different surface features (snow and ice), the reported mass change uncertainty encompasses errors arising from the lack of in-situ density observations and the inherent heterogeneity of snow layering, firn compaction, and melt–refreeze processes. Due to lack of high-resolution velocity data and ice thickness, ice flux contributions are not accounted in mass change estimation and hence could not calculate mass balance. Future work could extend UAV-based mass balance/change monitoring at glacier scale within the Antarctic Ice Sheet, such as Anuchin Glacier and other glaciers (inland or marine terminating) near the DML or other parts of Antarctica, to evaluate spatial variability in mass change across different glaciological settings. Incorporating diverse UAV payloads such as LiDAR (Light Detection and Ranging), thermal, etc., would enable enhanced characterization of surface conditions, snow properties, and provide a more comprehensive understanding of mass balance processes. Additionally, the deployment of coordinated UAV swarms presents a promising avenue for substantially increasing spatial coverage, allowing rapid acquisition of high-resolution data over larger areas of the ice sheet and improving the operational feasibility of UAV-based monitoring in polar regions.

Another key future direction involves integrating UAV-derived datasets with satellite-based observations (e.g., ICESat-2, CryoSat-2, Sentinel-1 or 2) through multi-sensor fusion. By combining high-resolution UAV payloads (e.g., optical, multispectral, thermal, and/or LiDAR) with satellite altimetry and imagery, it becomes possible to bridge the spatial-temporal scale gap between in situ measurements and regional-scale remote sensing products. A recent study by Platel et al., (2025) highlighted the multi-sensor data fusion technique in monitoring polar vegetation. UAV surveys, if executed with consistent protocols and accurate positioning, can also serve as critical calibration and validation datasets for satellite-derived mass change products such as altimetry datasets from ICESat-2, or CryoSat-2. Such synergistic approaches will not only strengthen confidence in remote-sensing methods but also enhance accurate monitoring of ice-sheet evolution under changing climate conditions.

Conclusion

This study demonstrates the potential of UAV-based surveys for understanding Antarctic ice sheet surface processes. High-resolution UAV-derived data allow detailed characterization of surface features and enable the detection of subtle changes at short temporal scales, which are often missed by conventional measurements. Such datasets if collected regularly, provide valuable insights into sub-seasonal and seasonal variations in geodetic mass change and can serve as reliable validation and calibration sites for satellite-derived mass change products. Our results highlight that the short-term meteorological variabilities, including temperature fluctuations, snowfall, and wind gusts, strongly influence seasonal mass change by altering snow distribution over ice, whereas annual mass change is primarily governed by surface melt and snow accumulation patterns.

https://doi.org/10.5194/egusphere-2025-5601
Preprint. Discussion started: 5 March 2026

We also found surface terrain's aspect having strong control over the variations in mass change across the study site. Upon validation with in-situ stake-based elevation change measurements, our results aligned very well, showing its reliability. While operational challenges in deploying UAVs in Antarctica remain considerable, the study outlines practical recommendations to improve reliability and efficiency. UAV surveys using advanced payloads and multi-drone swarms offer promising opportunities to expand coverage across larger and more diverse regions of the Antarctic Ice Sheet or other polar environments.

Author contribution. All authors participated in field data collection (Investigation). A.G. led the Conceptualization, Methodology, Data curation, Formal analysis, and Writing (original draft preparation), preparing the methods, data processing, analysis, conclusion, and parts of the introduction and discussion. N.P.J. contributed to Formal analysis, Visualization, Investigation, and Writing (review and editing), preparing the results, figures, and discussion sections. T.G. contributed to Writing (original draft preparation) and Writing (review and editing), focusing on the introduction, manuscript structure, and final draft flow. R.R. was responsible for Funding acquisition, Project administration, Supervision, Investigation, and Writing (review and editing), providing guidance throughout the study and contributing to revisions across all sections. All authors reviewed and approved the final version of the manuscript.

Data availability: Upon manuscript acceptance, the UAV-derived digital elevation models (DEMs) and orthoimages produced and analyzed in this study, along with related metadata (coordinate reference system, ground control information, and processing parameters), will be deposited in a public repository aligned with FAIR (e.g., Zenodo) and given a DOI. The data may be made accessible to reviewers through the Copernicus review system (access restricted to reviewers) prior to public release.

Competing interest. All the authors declare they have no conflict of interest.

Financial Support. This project was supported by the National Centre for Polar and Ocean Research (NCPOR), Ministry of Earth Sciences, Government of India, under India's Antarctica program. No direct fundings were provided.

Acknowledgement. The authors acknowledge the support provided by the National Centre for Polar and Ocean Research (NCPOR), particularly the Antarctic Science Division team. We thank Mr. Sanjay Saifi and other members of the Hydro-Remote Sensing Applications Group (H-RSA) at the Indian Institute of Technology Bombay (IIT Bombay) for their valuable assistance. We also thank India Meteorological Department (IMD) for providing Meteorological data. The authors also acknowledge the Geological Survey of India (GSI) and all members and station leaders of the 43rd and 44th Indian Scientific Expeditions to Antarctica (ISEA) for their logistical and field assistance.

https://doi.org/10.5194/egusphere-2025-5601
Preprint. Discussion started: 5 March 2026

Declaration of Generative AI and AI-assisted technologies in the writing process

During the preparation of this work, the authors used ChatGPT 5 to assist with rephrasing and improving the clarity of the manuscript's language. All content was carefully reviewed and edited by the authors to ensure its accuracy and completeness. The authors take full responsibility for the final version of the publication.

References

Agisoft Metashape: https://www.agisoft.com/, last access: 14 July 2025.

Amory, C., Kittel, C., Le Toumelin, L., Agosta, C., Delhasse, A., Favier, V., and Fettweis, X.: Performance of MAR (v3.11) in simulating the drifting-snow climate and surface mass balance of Adélie Land, East Antarctica, Geosci. Model Dev., 14, 3487–3510, https://doi.org/10.5194/gmd-14-3487-2021, 2021.

Bello, C., Suarez, W., and Brondi, F.: Determining the geodetic mass balance of the Znosko glacier (King George Island, Antarctica) using an unmanned aerial vehicle, Remote Sens. Lett., 14, 148–156, https://doi.org/10.1080/2150704X.2023.2165419, 2023.

Bhardwaj, A., Sam, L., Akanksha, Martín-Torres, F. J., and Kumar, R.: UAVs as remote sensing platform in glaciology: Present applications and future prospects, Remote Sens. Environ., 175, 196–204, https://doi.org/10.1016/j.rse.2015.12.029, 2016.

Birnbaum, G., Freitag, J., Brauner, R., König-Langlo, G., Schulz, E., Kipfstuhl, S., Oerter, H., Reijmer, C. H., Schlosser, E., Faria, S. H., Ries, H., Loose, B., Herber, A., Duda, M. G., Powers, J. G., Manning, K. W., and Van Den Broeke, M. R.: Strong-wind events and their influence on the formation of snow dunes: observations from Kohnen station, Dronning Maud Land, Antarctica, J. Glaciol., 56, 891–902, https://doi.org/10.3189/002214310794457272, 2010.

Bliakharskii, D. P., Florinsky, I. V., and Skrypitsyna, T. N.: Modelling glacier topography in Antarctica using unmanned aerial survey: assessment of opportunities, Int. J. Remote Sens., 40, 2517–2541, https://doi.org/10.1080/01431161.2019.1584926, 2019.

Cuffey, K. M. and Paterson, W. S. B.: The physics of glaciers, 4. ed., Butterworth-Heineman, Amsterdam Heidelberg, 693 pp., 2010.

https://doi.org/10.5194/egusphere-2025-5601
Preprint. Discussion started: 5 March 2026

DeConto, R. M. and Pollard, D.: Contribution of Antarctica to past and future sea-level rise, Nature, 531, 591–597, https://doi.org/10.1038/nature17145, 2016.

Edwards, T. L., Nowicki, S., Marzeion, B., Hock, R., Goelzer, H., Seroussi, H., Jourdain, N. C., Slater, D. A., Turner, F. E., Smith, C. J., McKenna, C. M., Simon, E., Abe-Ouchi, A., Gregory, J. M., Larour, E., Lipscomb, W. H., Payne, A. J., Shepherd, A., Agosta, C., Alexander, P., Albrecht, T., Anderson, B., Asay-Davis, X., Aschwanden, A., Barthel, A., Bliss, A., Calov, R., Chambers, C., Champollion, N., Choi, Y., Cullather, R., Cuzzone, J., Dumas, C., Felikson, D., Fettweis, X., Fujita, K., Galton-Fenzi, B. K., Gladstone, R., Golledge, N. R., Greve, R., Hattermann, T., Hoffman, M. J., Humbert, A., Huss, M., Huybrechts, P., Immerzeel, W., Kleiner, T., Kraaijenbrink, P., Le Clec'H, S., Lee, V., Leguy, G. R., Little, C. M., Lowry, D. P., Malles, J.-H., Martin, D. F., Maussion, F., Morlighem, M., O'Neill, J. F., Nias, I., Pattyn, F., Pelle, T., Price, S. F., Quiquet, A., Radić, V., Reese, R., Rounce, D. R., Rückamp, M., Sakai, A., Shafer, C., Schlegel, N.-J., Shannon, S., Smith, R. S., Straneo, F., Sun, S., Tarasov, L., Trusel, L. D., Van Breedam, J., Van De Wal, R., Van Den Broeke, M., Winkelmann, R., Zekollari, H., Zhao, C., Zhang, T., and Zwinger, T.: Projected land ice contributions to twenty-first-century sea level rise, Nature, 593, 74–82, https://doi.org/10.1038/s41586-021-03302-y, 2021.

Engel, Z., Láska, K., Nývlt, D., and Stachoň, Z.: Surface mass balance of small glaciers on James Ross Island, north-eastern Antarctic Peninsula, during 2009–2015, J. Glaciol., 64, 349–361, https://doi.org/10.1017/jog.2018.17, 2018.

Florinsky, I. V. and Bliakharskii, D. P.: Detection of crevasses by geomorphometric treatment of data from unmanned aerial surveys, Remote Sens. Lett., 10, 323–332, https://doi.org/10.1080/2150704X.2018.1552809, 2019.

Fischer, M., Huss, M., and Hoelzle, M.: Surface elevation and mass changes of all Swiss glaciers 1980–2010, The Cryosphere, 9, 525–540, https://doi.org/10.5194/tc-9-525-2015, 2015.

Fretwell, P., Pritchard, H. D., Vaughan, D. G., Bamber, J. L., Barrand, N. E., Bell, R., Bianchi, C., Bingham, R. G., Blankenship, D. D., Casassa, G., Catania, G., Callens, D., Conway, H., Cook, A. J., Corr, H. F. J., Damaske, D., Damm, V., Ferraccioli, F., Forsberg, R., Fujita, S., Gogineni, P., Griggs, J. A., Hindmarsh, R. C. A., Holmlund, P., Holt, J. W., Jacobel, R. W., Jenkins, A., Jokat, W., Jordan, T., King, E. C., Kohler, J., Krabill, W., Riger-Kusk, M., Langley, K. A., Leitchenkov, G., Leuschen, C., Luyendyk, B. P., Matsuoka, K., Nogi, Y., Nost, O. A., Popov, S. V., Rignot, E., Rippin, D. M., Riviera, A., Roberts, J., Ross, N., Siegert, M. J., Smith, A. M., Steinhage, D., Studinger, M., Sun, B., Tinto, B. K., Welch, B. C., Young, D. A., Xiangbin, C., and Zirizzotti, A.: Bedmap2: improved ice bed, surface and thickness datasets for Antarctica, https://doi.org/10.5194/tcd-6-4305-2012, 11 October 2012.

https://doi.org/10.5194/egusphere-2025-5601
Preprint. Discussion started: 5 March 2026

Garg, S., Navinkumar, P. J., Godara, A., Sahu, R., Singh, D. K., and Ramsankaran, R.: Remote sensing the evolution of debris-covered Panchi Nala-A glacier, India (1971-2021) from satellites and Unmanned Aerial Vehicles, Reg. Environ. Change, 23, 103, https://doi.org/10.1007/s10113-023-02096-1, 2023.

Gindraux, S., Boesch, R., and Farinotti, D.: Accuracy Assessment of Digital Surface Models from Unmanned Aerial Vehicles' Imagery on Glaciers, Remote Sens., 9, 186, https://doi.org/10.3390/rs9020186, 2017.

Huss, M.: Density assumptions for converting geodetic glacier volume change to mass change, The Cryosphere, 7, 877–887, https://doi.org/10.5194/tc-7-877-2013, 2013.

Immerzeel, W. W., Kraaijenbrink, P. D. A., Shea, J. M., Shrestha, A. B., Pellicciotti, F., Bierkens, M. F. P., and De Jong, S. M.: High-resolution monitoring of Himalayan glacier dynamics using unmanned aerial vehicles, Remote Sens. Environ., 150, 93–103, https://doi.org/10.1016/j.rse.2014.04.025, 2014.

Ipcc: The Ocean and Cryosphere in a Changing Climate: Special Report of the Intergovernmental Panel on Climate Change, 1st ed., Cambridge University Press, https://doi.org/10.1017/9781009157964, 2022.

Lenaerts, J. T. M., Van Meijgaard, E., Van Den Broeke, M. R., Ligtenberg, S. R. M., Horwath, M., and Isaksson, E.: Recent snowfall anomalies in Dronning Maud Land, East Antarctica, in a historical and future climate perspective, Geophys. Res. Lett., 40, 2684–2688, https://doi.org/10.1002/grl.50559, 2013.

Lenaerts, J. T. M., Vizcaino, M., Fyke, J., Van Kampenhout, L., and Van Den Broeke, M. R.: Present-day and future Antarctic ice sheet climate and surface mass balance in the Community Earth System Model, Clim. Dyn., 47, 1367–1381, https://doi.org/10.1007/s00382-015-2907-4, 2016.

Leuschen, C., Hale, R., Keshmiri, S., Yan, J. B., Rodriguez-Morales, F., Mahmood, A., and Gogineni, S.: UAS-Based Radar Sounding of the Polar Ice Sheets, IEEE Geosci. Remote Sens. Mag., 2, 8–17, https://doi.org/10.1109/MGRS.2014.2306353, 2014.

Markov, A., Polyakov, S., Sun, B., Lukin, V., Popov, S., Yang, H., Zhang, T., Cui, X., Guo, J., Cui, P., Zhang, L., Greenbaum, J., Mirakin, A., Voyevodin, A., Boronina, A., Sukhanova, A., Deshovykh, G., Krekhov, A., Zarin, S.,

https://doi.org/10.5194/egusphere-2025-5601
Preprint. Discussion started: 5 March 2026

Semyonov, A., Soshchenko, V., and Mel'nik, A.: The conditions of the formation and existence of "Blue Ice Areas" in the ice flow transition region from the Antarctic ice sheet to the Amery Ice Shelf in the Larsemann Hills area, Polar Sci., 22, 100478, https://doi.org/10.1016/j.polar.2019.08.004, 2019.

Otosaka, I. N., Shepherd, A., Ivins, E. R., Schlegel, N.-J., Amory, C., Van Den Broeke, M. R., Horwath, M., Joughin, I., King, M. D., Krinner, G., Nowicki, S., Payne, A. J., Rignot, E., Scambos, T., Simon, K. M., Smith, B. E., Sørensen, L. S., Velicogna, I., Whitehouse, P. L., A, G., Agosta, C., Ahlstrøm, A. P., Blazquez, A., Colgan, W., Engdahl, M. E., Fettweis, X., Forsberg, R., Gallée, H., Gardner, A., Gilbert, L., Gourmelen, N., Groh, A., Gunter, B. C., Harig, C., Helm, V., Khan, S. A., Kittel, C., Konrad, H., Langen, P. L., Lecavalier, B. S., Liang, C.-C., Loomis, B. D., McMillan, M., Melini, D., Mernild, S. H., Mottram, R., Mouginot, J., Nilsson, J., Noël, B., Pattle, M. E., Peltier, W. R., Pie, N., Roca, M., Sasgen, I., Save, H. V., Seo, K.-W., Scheuchl, B., Schrama, E. J. O., Schröder, L., Simonsen, S. B., Slater, T., Spada, G., Sutterley, T. C., Vishwakarma, B. D., Van Wessem, J. M., Wiese, D., Van Der Wal, W., and Wouters, B.: Mass balance of the Greenland and Antarctic ice sheets from 1992 to 2020, Earth Syst. Sci. Data, 15, 1597–1616, https://doi.org/10.5194/essd-15-1597-2023, 2023.

Pina, P. and Vieira, G.: UAVs for Science in Antarctica, Remote Sens., 14, 1610, https://doi.org/10.3390/rs14071610, 2022.

Platel, A., Sandino, J., Shaw, J., Bollard, B., and Gonzalez, F.: Advancing Sparse Vegetation Monitoring in the Arctic and Antarctic: A Review of Satellite and UAV Remote Sensing, Machine Learning, and Sensor Fusion, Remote Sens., 17, 1513, https://doi.org/10.3390/rs17091513, 2025.

Rignot, E., Mouginot, J., Scheuchl, B., Van Den Broeke, M., Van Wessem, M. J., and Morlighem, M.: Four decades of Antarctic Ice Sheet mass balance from 1979–2017, Proc. Natl. Acad. Sci., 116, 1095–1103, https://doi.org/10.1073/pnas.1812883116, 2019.

Rolstad, C., Haug, T., and Denby, B.: Spatially integrated geodetic glacier mass balance and its uncertainty based on geostatistical analysis: application to the western Svartisen ice cap, Norway, J. Glaciol., 55, 666–680, https://doi.org/10.3189/002214309789470950, 2009.

Rounce, D. R., Hock, R., Maussion, F., Hugonnet, R., Kochtitzky, W., Huss, M., Berthier, E., Brinkerhoff, D., Compagno, L., Copland, L., Farinotti, D., Menounos, B., and McNabb, R. W.: Global glacier change in the 21st century: Every increase in temperature matters, Science, 379, 78–83, https://doi.org/10.1126/science.abo1324, 2023.

Schlosser, E. and Oerter, H.: Shallow firn cores from Neumayer, Ekströmisen, Antarctica: a comparison of accumulation rates and stable-isotope ratios, Ann. Glaciol., 35, 91–96, https://doi.org/10.3189/172756402781816915, 2002.

https://doi.org/10.5194/egusphere-2025-5601
Preprint. Discussion started: 5 March 2026

Sinharay, R. K.: Ground Penetrating Radar (GPR) survey over a melting blue ice area (BIA) at the south of Schirmacher Oasis, Dronning Maud Land, East Antarctica, Polar Sci., 32, 100845, https://doi.org/10.1016/j.polar.2022.100845, 2022.

Sinharay, R. K.: Ground Penetrating Radar (GPR) survey over a melting blue ice area (BIA) at the south of Schirmacher Oasis, Dronning Maud Land, East Antarctica, Polar Sci., 32, 100845, https://doi.org/10.1016/j.polar.2022.100845, 2022.

Sunil PS, Reddy CD, Ponraj M, Dhar A and Jayapaul D (2007) GPS determination of the velocity and strain-rate fields on Schirmacher Glacier, central Dronning Maud Land, Antarctica. Journal of Glaciology 53(183), 558–564. doi:10.3189/002214307784409199.

Sutter, J., Gierz, P., Grosfeld, K., Thoma, M., and Lohmann, G.: Ocean temperature thresholds for Last Interglacial West Antarctic Ice Sheet collapse, Geophys. Res. Lett., 43, 2675–2682, https://doi.org/10.1002/2016GL067818, 2016.

Thiery, W., Gorodetskaya, I. V., Bintanja, R., Van Lipzig, N. P. M., Van Den Broeke, M. R., Reijmer, C. H., and Kuipers Munneke, P.: Surface and snowdrift sublimation at Princess Elisabeth station, East Antarctica, The Cryosphere, 6, 841–857, https://doi.org/10.5194/tc-6-841-2012, 2012.

Thiery, W., Gorodetskaya, I. V., Bintanja, R., Van Lipzig, N. P. M., Van den Broeke, M. R., Reijmer, C. H., and Kuipers Munneke, P.: Surface and snowdrift sublimation at Princess Elisabeth station, East Antarctica, The Cryosphere, 6, 841–857, https://doi.org/10.5194/tc-6-841-2012, 2012.

Winther, J.-G., Elvehøy, H., Bøggild, C. E., Sand, K., and Liston, G.: Melting, runoff and the formation of frozen lakes in a mixed snow and blue-ice field in Dronning Maud Land, Antarctica, J. Glaciol., 42, 271–278, https://doi.org/10.3189/S0022143000004135, 1996.

Yu, L., Zhong, S., Jagovkina, S., Sui, C., and Sun, B.: Interannual Variability and Trends in Extreme Precipitation in Dronning Maud Land, East Antarctica, Remote Sens., 17, 324, https://doi.org/10.3390/rs17020324, 2025.